Near-field images of a monolayer of periodically arrayed dielectric spheres

Near-field images of a monolayer of periodically arrayed dielectric spheres

Hiroshi Miyazaki*

Department of Applied Physics, School of Engineering, Tohoku University, Aramaki, Aoba-ku, Sendai 980-8579, Japan

Kazuo Ohtaka

Department of Applied Physics, Faculty of Engineering, Chiba University, 1-33 Yayoi, Inage-ku, Chiba 263-8522, Japan

(Received 29 December 1997)

A theoretical analysis is given for the near-field images of a monolayer of periodically arrayed dielectric spheres, obtained by monochromatic external light. Depending on the frequency and the incident angle of exciting light, the near-field intensity exhibits a large enhancement due to the resonant excitation of photonic bands with two-dimensional band dispersion. The various near-field patterns, sometimes quite unlike the image by natural light, are shown to occur and are analyzed using the plane-wave amplitudes of excited Bloch waves. The resonant pattern is well understood by the group-theoretical characters of photonic bands. Also, an analytical expression is given for the field in the long wavelength limit, which can reproduce all the numerical characteristics quite successfully. Especially, it can explain why the near-field image becomes ω independent, while the reflectivity varies as ω^2. [S0163-1829(98)05935-9]

I. INTRODUCTION

Recently dielectric objects arrayed periodically, called photonic crystals, have attracted much attention.[1] The interest mainly originates from technological incentives of using the photonic states of such systems in optically controlling the electron dynamics. Photonic band structure appears as a result of periodic modulation of the dielectric constant, and resembles in many ways the more familiar electronic band structures of ordinary solid state systems. There is a long history of research of the properties of one-dimensional (1D) photonic crystals, periodic multilayer stacks in one direction. Their peculiar frequency ranges of total reflection are now well understood in the photonic-band picture. A typical example of 2D or 3D photonic crystals is a periodic array of polymer spheres formed in aqueous suspensions. Such a system of microspheres provides us with the field for photons of visible range that plays the role of periodic array of atoms for electrons in ordinary solids. As an electron hops from atom to atom to form a tight-binding band, the same phenomenon occurs in the photonic case. Though the formulation for the photonic band theory and the optical response of such systems were completed in the late 1970s and early 1980s,[2–4] systematic research of 2D and 3D photonic crystals has not been carried out until recently, when people realized a variety of their technological applications such as single-mode light-emitting diodes[5] and optical waveguides with high resolution.[6]

A variety of periodic structures of 2D and 3D photonic crystals, in size and shape of arrayed units, have been proposed, fabricated, and investigated extensively both theoretically and experimentally.[1,7,8] However, the efforts to date have been restricted to the search for a photonic crystal, which has an absolute band gap prohibiting the electromagnetic propagation in all directions. Of course this situation is desirable from a technological point of view, but photonic bands have in themselves many physical properties worthy of fundamental investigation. One of them is the massiveness

of photons in photonic crystals, which stems from their property as a coherent hopping mode of localized states, i.e., just an electromagnetic version of heavy fermions.

Most of the theoretical treatments have so far been based on the expansion of the Bloch electromagnetic fields in terms of plane waves. Although this method is handy and applies widely, it has a limitation of very slow convergence.[9,10] The formulation due to one of the authors (K.O.) is to use the completeness relation of the set of vector spherical and cylindrical waves in the system of arrayed spheres and cylinders.[2,10] This is conceptually a natural extension of the familiar approach for electrons to photons. Making use of the much faster convergence and greater accuracy, he examined various optical properties of photonic bands and explained successfully how they change from band to band depending on the individual band characteristics.[11–14] These previous works were mainly concerned with the far-field properties of photonic bands, i.e., such properties as involved in the reflectivity or transimittivity observed by a detector far away from the photonic crystals.

The present paper treats the near-field properties of photonic bands, for a single layer of 2D periodic array of spheres. Near-field optics attracts growing attention because of its remarkably high spatial resolution.[15,16] Though some analyses based upon Fourier decomposition are found for grating geometries,[17–20] the near-field optics for the periodic system has not yet been discussed in relation to the photonic bands.

A monolayer system of 2D periodicity has two mutually contrasting characteristics: it is a closed system in the lateral plane and is an open system in the third direction. Therefore, a photon behaves therein as a heavy photon in the lateral motion but presents simultaneously a dissipative behavior in the third direction. The dissipation is caused by leakage of electromagnetic energy into the surrounding free space and accordingly is the origin of the coupling between the eigenmodes of the monolayer and the plane-wave states of the external world. A photonic band couples to an external

plane-wave probe through this mechanism. The near-field response to an external probe thus provides us with fruitful information on the photonic bands. The purpose of this paper is to show in a quantitative way how the near-field image is indeed explained by the properties of photonic bands.

The near-field is examined by SNOM (scanning near-field optical microscopy).[21] In this paper we restrict ourselves to the field excited near the system by an external plane-wave light, which we shall often call ''the local field.'' As analyzed in Ref. 22, the time-reversal symmetry shows that the intensity of the local field at a point near the specimen is nothing but the field that is obtained at infinity, using the probing light coming in the reverse direction from a point source placed where the local field is measured. By a point source we mean here the SNOM tip. The analysis of the present paper will show that the monolayer system can potentially be used as a standard measure of the resolution of SNOM, because this system allows a thorough study using the concept of photonic bands, as done in this paper. Also the near-field image in the long wavelength limit, i.e., that obtained by the light of wavelength much larger than the periodicity of the array, is shown to be given by a compact analytical expression.

In Sec. II, we summarize the formulation of the light scattering from a monolayer of spheres to obtain the near-field expression. Section III is devoted to the numerical presentation of the reflectivity spectrum and near-field images. We restrict ourselves to the resonant features in this section. The interpretation in relation to the dissipative 2D photonic band is also introduced. In Sec. IV, we attempt to reproduce the resonant near-field images discussed in Sec. III by using the group-theoretical knowledge of 2D photonic bands. Section V deals with the light scattering in the long wavelength limit. Short comments in Sec. VI conclude the paper.

II. MODEL AND FIELD EQUATIONS

We consider a single layer of periodically arrayed dielectric spheres in free space. Each sphere has a uniform dielectric constant ε and radius a. The origin of the coordinates is taken at the center of one of the spheres and the xy plane is chosen to be the plane of the monolayer, with the z axis normal to the plane. Let the plane-wave electromagnetic field of wave vector $\mathbf{k}_0$ be incident from below the layer ($z<0$):

$$\mathbf{E}(\mathbf{r})=\mathbf{E}^0\exp(i\mathbf{k}_0\cdot\mathbf{r}), \qquad (2.1)$$

where

$$\mathbf{k}_0=(\mathbf{k},\Gamma_0^+) \quad\text{and}\quad \Gamma_0^\pm=\pm\sqrt{(\mathbf{k}_0)^2-(\mathbf{k})^2}, \qquad (2.2)$$

$\mathbf{k}=(\mathbf{k}_x,\mathbf{k}_y)$ and Γ_0^+ being the in-plane and z components of $\mathbf{k}_0$, respectively. Throughout the present paper we consider only the electric field.

The incident photon suffers from multiple scattering in the layer and hops from sphere to sphere. It emerges finally out of the monolayer with an in-plane wave vector $\mathbf{k}+\mathbf{h}$, $\mathbf{h}$ being a 2D reciprocal lattice vector acquired by umklapp scattering. The transmitted and reflected fields are expressed

as a sum of the plane waves specified by various $\mathbf{h}$. Let $\mathbf{k}_\mathbf{h}^\pm$ be the 3D wave vector of the outgoing $\mathbf{h}$ wave. By energy conservation,

$$\mathbf{k}_\mathbf{h}^\pm=(\mathbf{k}+\mathbf{h},\Gamma_\mathbf{h}^\pm) \quad\text{and}\quad \Gamma_\mathbf{h}^\pm=\pm\sqrt{(\mathbf{k}_0)^2-(\mathbf{k}+\mathbf{h})^2}. \qquad (2.3)$$

Here the square root is chosen to be positive imaginary when its argument is negative and the superscripts $+$ and $-$ correspond to the transmitted (to be observed in the region $z>0$) and reflected ($z<0$) fields, respectively.

The scattering channel specified by $\mathbf{h}$ is called open (closed) when $\Gamma_\mathbf{h}^\pm$ is real (imaginary). Only the channel of $\mathbf{h}=\mathbf{0}$ is always open. The others have their threshold frequencies for the channel opening. The open channels carry away the energy in the direction of $\mathbf{k}_\mathbf{h}^\pm$ from the monolayer and determine the far-field intensity of the scattered field. They satisfy the unitarity condition, i.e., the flux conservation in the z direction. The closed channels, on the other hand, are specified by evanescent waves, their Poynting vector being directed in the lateral direction. They are not involved in flux conservation in the z direction, and hence their amplitudes can be arbitrarily large. The closed channels thus play a dominant role in the enhancement of the field intensity near the monolayer.

To express compactly the fields outside the system of spheres, we introduce transmission and reflection amplitudes $T_{ij}(\mathbf{hh}')$ and $R_{ij}(\mathbf{hh}')$, respectively. The quantity $T_{ij}(\mathbf{hh}')$ is the transmission amplitude of the jth Cartesian component of the incoming plane wave of wave vector $\mathbf{k}_{\mathbf{h}'}^+$ into the i component of the outgoing plane wave of $\mathbf{k}_\mathbf{h}^+$. $R_{ij}(\mathbf{hh}')$ describes similarly the reflection of the incoming $\mathbf{k}_{\mathbf{h}'}^+$ wave into the $\mathbf{k}_\mathbf{h}^-$ wave. In terms of them, the ith component of the electric fields outside the monolayer is expressed as

$$E_i(\mathbf{r})=\begin{cases} \displaystyle\sum_{\mathbf{h},j} T_{ij}(\mathbf{h0})\exp(i\mathbf{k}_\mathbf{h}^+\cdot\mathbf{r})E_j^0 & \text{for } z>0, \\ \displaystyle\sum_{\mathbf{h},j} R_{ij}(\mathbf{h0})\exp(i\mathbf{k}_\mathbf{h}^-\cdot\mathbf{r})E_j^0 & \text{for } z<0, \end{cases} \qquad (2.4)$$

where the summation over $\mathbf{h}$ covers all possible channels, open or closed. To express the flux continuity in the z direction, we introduce the total transmission and reflection coefficients, $\mathcal{T}$ and $\mathcal{R}$, defined by

$$\mathcal{T}=\sum_\mathbf{h}' \left(\sum_i \left|\sum_j T_{ij}(\mathbf{h0})E_j^0\right|^2\right)\cos(\hat{\mathbf{k}}_\mathbf{h}^+\cdot\hat{\mathbf{z}}),$$
$$\mathcal{R}=\sum_\mathbf{h}' \left(\sum_i \left|\sum_j R_{ij}(\mathbf{h0})E_j^0\right|^2\right)\cos(\hat{\mathbf{k}}_\mathbf{h}^+\cdot\hat{\mathbf{z}}). \qquad (2.5)$$

Here, the primed summation is only over $\mathbf{h}$ of open channels and the vectors with carets are unit vectors. Then, for the incident field of unit amplitude, the continuity of the z component of the incoming and outgoing Poynting vectors is expressed by

$$\mathcal{T}+\mathcal{R}=\cos(\hat{\mathbf{k}}_0\cdot\hat{\mathbf{z}}). \qquad (2.6)$$

This identity serves as a check of the numerical procedure. Note that the lack of the mixing between different $\mathbf{h}$ in these formulas is due to the integral in a lateral plane over the 2D unit cell.

In the frequency range in which only the channel 0 is open $\mathcal{T}$ and $\mathcal{R}$ are given by

$$\mathcal{T} = \sum_i \left| \sum_j T_{ij}(\mathbf{00})E_j^0 \right|^2 \cos(\hat{\mathbf{k}}_0 \cdot \hat{\mathbf{z}}),$$

$$\mathcal{R} = \sum_i \left| \sum_j R_{ij}(\mathbf{00})E_j^0 \right|^2 \cos(\hat{\mathbf{k}}_0 \cdot \hat{\mathbf{z}}), \tag{2.7}$$

which describe direct transmission and specular reflection, respectively.

The transmission and reflection amplitudes $T_{ij}(\mathbf{hh'})$ and $R_{ij}(\mathbf{hh'})$ involved in Eq. (2.5) or Eq. (2.7) are obtained by expanding the incident and scattered fields in terms of the vector spherical fields of $^M\mathbf{E}_{lm}(\mathbf{r})$ and $^N\mathbf{E}_{lm}(\mathbf{r})$, in the notation of Stratton.[23] Multiple scattering within a sphere is taken into account by the intrasphere t matrix. The multiple scattering in the periodic array as a whole is then expressed as an infinite series of the intrasphere scattering followed by the photon propagation between spheres. Finally, converting the spherical waves into the sum of the outgoing plane waves yields $T_{ij}(\mathbf{hh'})$ and $R_{ij}(\mathbf{hh'})$. The details of the mathematical procedure are given in Ref. 4, and we simply quote the final expressions:

$$T_{ii'}(\mathbf{hh'}) = \delta_{ii'}\delta_{\mathbf{hh'}} + \frac{\gamma_0}{\Gamma_{\mathbf{h}}^+} \mathbf{Y}^t(\hat{\mathbf{k}}_{\mathbf{h}}^+)\boldsymbol{\tau}_{ii'}\mathbf{Y}^*(\hat{\mathbf{k}}_{\mathbf{h'}}^+),$$

$$\tag{2.8}$$

$$R_{ii'}(\mathbf{hh'}) = \frac{\gamma_0}{\Gamma_{\mathbf{h}}^+}\mathbf{Y}^t(\hat{\mathbf{k}}_{\mathbf{h}}^-)\boldsymbol{\tau}_{ii'}\mathbf{Y}^*(\hat{\mathbf{k}}_{\mathbf{h'}}^+).$$

Here, the first term of $T_{ii'}(\mathbf{hh'})$ represents the incident plane wave when $\mathbf{h'}=\mathbf{0}$, and $\gamma_0 = -i/S$, S being the area of the unit cell. $\mathbf{Y}(\hat{\mathbf{k}}_{\mathbf{h}}^-)$ is a vertical array of the spherical harmonics: $\mathbf{Y}(\hat{\mathbf{k}}_{\mathbf{h}}^-) = \{Y_{00}(\hat{\mathbf{k}}_{\mathbf{h}}^-), Y_{1-1}(\hat{\mathbf{k}}_{\mathbf{h}}^-), Y_{10}(\hat{\mathbf{k}}_{\mathbf{h}}^-), Y_{11}(\hat{\mathbf{k}}_{\mathbf{h}}^-), \ldots\}^t$. $\mathbf{Y}(\hat{\mathbf{k}}_{\mathbf{h}}^+)$ is similarly defined. Note that the z component of $\hat{\mathbf{k}}_{\mathbf{h}}^\pm$ of closed channels is imaginary in the arguments of the spherical harmonics. The matrices $\boldsymbol{\tau}_{ij}$ are given by

$$\boldsymbol{\tau}_{ij} = \mathbf{U}^* \left(\sum_{\beta\beta'} \mathbf{P}_i^\beta \boldsymbol{\tau}^{\beta\beta'}\mathbf{L}(\mathbf{P}_j^{\beta'})^\dagger \right)\mathbf{U}, \tag{2.9}$$

where the sum runs over $\beta = M$ and N (likewise for β') and the matrix elements of $\mathbf{U}$ and $\mathbf{L}$ are given by $(\mathbf{U})_{lm;l'm'} = 4\pi i^l \delta_{ll'}\delta_{mm'}$ and $(\mathbf{L})_{lm;l'm'} = \delta_{ll'}\delta_{mm'}/[l(l+1)]$. The matrix $\mathbf{P}_j^\beta$ gives the expansion coefficients of the jth component of the vector spherical waves into the spherical harmonics. They are written in terms of the Clebsch-Gordan coefficients.[2] In the matrix element $(\mathbf{P}_j^\beta)_{lm;l'm'}$, l runs over $l \geq 0$ but l' over $l' \geq 1$. The matrices $\boldsymbol{\tau}^{\beta\beta'}$ (there are four such matrices, $\boldsymbol{\tau}^{MM}$, $\boldsymbol{\tau}^{MN}$, etc.) are square matrices defined within the space $l, l' \geq 1$. They are the $(\beta\beta')$ block of the layer t matrix $\boldsymbol{\tau}$, defined by

$$\boldsymbol{\tau} = \begin{pmatrix} \mathbf{t}^M, & 0 \\ 0, & \mathbf{t}^N \end{pmatrix} \mathbf{B},$$
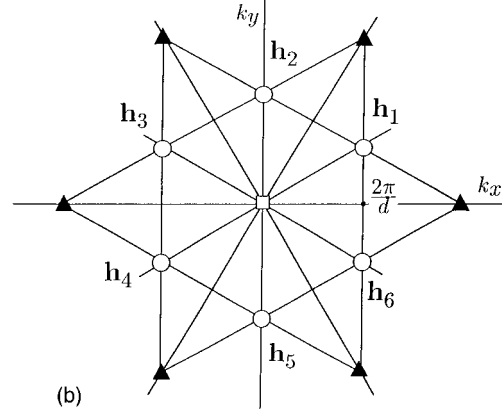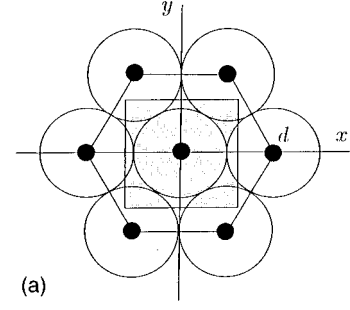

(a)

(b)

FIG. 1. Real (a) and reciprocal (b) spaces of triangular lattice. The shaded square of panel (a) is the region of (x,y) with $-0.6d \leq x, y \leq 0.6d$, where the local-field profile is displayed in this paper. In (b), the reciprocal lattice points $\mathbf{h}$ in the NN and 2NN shells are shown. Those in the NN shell are numbered for later purpose.

$$\mathbf{B} = \begin{pmatrix} \mathbf{I} - \boldsymbol{\gamma}^{MM}\mathbf{t}^M, & -\boldsymbol{\gamma}^{MN}\mathbf{t}^N \\ -\boldsymbol{\gamma}^{NM}\mathbf{t}^M, & \mathbf{I} - \boldsymbol{\gamma}^{NN}\mathbf{t}^N \end{pmatrix}^{-1}. \tag{2.10}$$

Here, $\mathbf{t}^\beta$ is the intrasphere t matrix and $\boldsymbol{\gamma}^{\beta\beta'}$ is the structure factor that specifies the light propagation between spheres. When expanded into a power series with respect to $\mathbf{t}^\beta$, $\boldsymbol{\tau}$ is seen to involve an infinite sequence of Mie scattering. Its off-diagonal blocks $\boldsymbol{\tau}^{MN}$ and $\boldsymbol{\tau}^{NM}$ describe the mixing between the M and N spherical waves in the course of scattering.

III. RESONANT NEAR-FIELD IMAGES

In this section, we present the numerical results of the reflectivity spectra and near-field images. We have in mind the experiment of SNOM on a single layer of polystyrene spheres of radius a and dielectric constant ε, which are arrayed in a triangular lattice of lattice constant d. We set $\varepsilon = 1.6^2$ and $a/d = 0.5$. The refractive index of 1.6 is that of polystyrene spheres in the visible range, and the second condition corresponds to the close-packed triangular lattice of spheres in contact with each other.

Figure 1 shows the geometry of the lattice. The shaded square is the region where the intensity map of the local field will be calculated. By the Bloch theorem the field-intensity outside the square is obtained by periodic extention. Panel (b) shows the reciprocal lattice with lattice constant $2/\sqrt{3}(2\pi/d)$, which is obtained by rotating the real-space
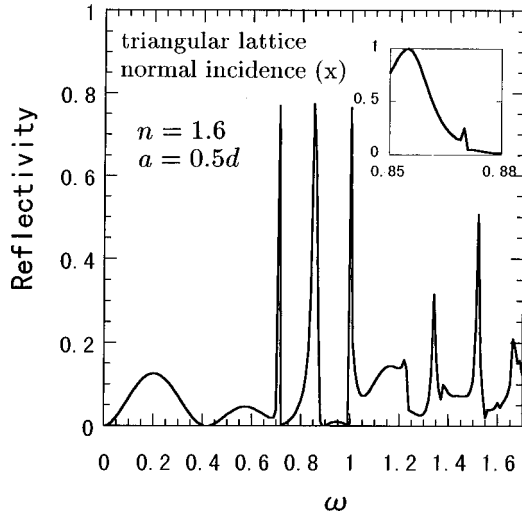
FIG. 2. Reflectivity $\mathcal{R}$ versus ω for the light in the normal incidence. The refractive index n and the radius a of spheres are $n = 1.6$ and $a = 0.5d$, d being the lattice constant. The inset is a closer look of $\mathcal{R}$ near $\omega = 0.85$, which shows the peak around $\omega = 0.85$ to be actually composed of two peaks.

lattice by $\pi/6$. We call a group of lattice points of equal length $|\mathbf{h}|$ as belonging to a shell of the reciprocal lattice points. The point $\mathbf{h} = 0$ defines by itself the first shell, which we shall call the 0 shell. Six lattice points nearest to the 0 shell form the second shell, which we call the NN (nearest-neighbor) shell. The third shell is called the 2NN (second-nearest-neighbor) shell. For later purpose, the lattice points of the NN shell are numbered in Fig. 1.

We consider the incident electric field of unit amplitude and wave vector $\mathbf{k}_0$ at normal and oblique incidence. In the oblique incidence we keep the wave vector $\mathbf{k}_0$ within the xz plane and tilt it from the z axis by the incidence angle θ. The incident light of s polarization is polarized in the y direction while that of p is within the xz plane. We employ this naming of s or p even for normal incidence by calling the y (x) polarized as s (p). We measure the wave number k in units of $2/\sqrt{3}(2\pi/d)$ and the frequency ω in units of c times this quantity, c being the light velocity. In terms of the wavelength λ of light in free space, k and ω are thus given by

$$k = \omega = \frac{\sqrt{3}d}{2\lambda}. \qquad (3.1)$$

For normal incidence the six channels for $\mathbf{h}$ in the NN shell open simultaneously at $\omega = 1$, and the channels of the 2NN shell open at $\omega = \sqrt{3}$. In the numerical results given below, a good convergence is achieved for $\omega < 1.7$ by considering $l \leq 8$.

A. Normal incidence

Let us start with the normal incidence case. Figure 2 shows the reflectivity $\mathcal{R}$, defined by Eq. (2.5), as a function of ω. By symmetry the result is identical for s and p polarizations. Sharp peaks arise at $\omega = 0.71$, 0.85, 1.00, 1.34, and 1.55. The asymmetry of the peak at $\omega = 0.85$ is due to the resolution-limited degeneracy, as shown in the inset obtained with a finer frequency step. We see that the peak is really a
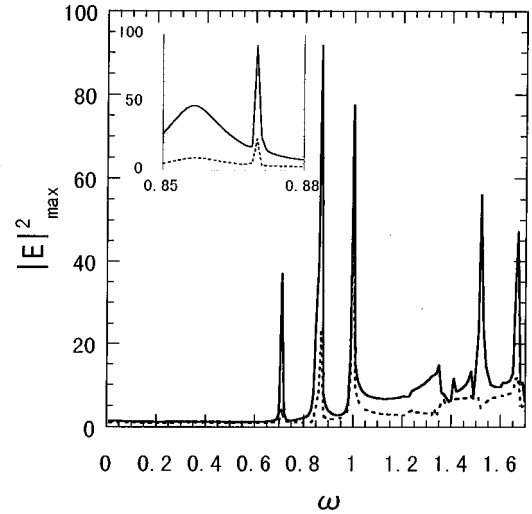

FIG. 3. Frequency dependence of the maximum intensity of near field. The solid line shows the maximum value on the sampling plane at $z = a$ and the dotted line on the plane at $z = 1.2a$. The incident light of normal incidence is p-polarized (polarized parallel to the x axis). The inset shows $\mathcal{R}$ around $\omega = 0.85$ with the enlarged horizontal scale.

doublet consisting of a broad peak at $\omega = 0.854$ and a sharp one at $\omega = 0.870$. The peak at $\omega = 1.00$ occurs at the threshold for the opening of the NN-shell channels. As analyzed in Ref. 24, the occurrence of such a peak is a textbook phenomenon observed at the frequency for channel opening.

The two broad peaks near the origin are similar in shape to the interference fringes of a uniform dielectric slab. We can in fact see that four, eight,... peaks appear with shorter periodicity in frequency, as 2,4,... layers are stacked to increase the thickness (see Ref. 11). It is remarkable that the Mie resonance due to spherical confinement, which is the origin of the series of sharp peaks of Fig. 2, is orders of magnitude sharper than these two peaks of the thin-film interference effects.

To check the coincidence between the peaks of the reflectivity and near-field intensity, we plot in Fig. 3 the frequency dependence of the maximum intensity of the local field $|\mathbf{E}(\mathbf{r})|^2$ on two sampling planes above the layer at $z = a$ (solid line) and $z = 1.2a$ (dotted line). By positive z we mean that the observation point $\mathbf{r}$ lies on the exit side. The frequency step is the same as that of Fig. 2.

Comparison of Fig. 3 with Fig. 2 shows that the peaks of the reflectivity and local-field intensity are positioned in exact agreement, including those of the doublet at $\omega = 0.85$. It is remarkable that the local-field intensity is sometimes as large as 10^2. This type of large enhancement is the same phenomenon as calculated for the 3D lattice of spheres.[12] A marked decrease of the local-field intensity at the plane $z = 1.2a$, as compared to that at $z = a$, is the third notable feature of Fig. 3. The rapid decrease obviously shows that the resonant enhancement is due predominantly to the evanescent waves from the closed channels. All these characteristics of the resonant peaks are similarly observed when the local field is calculated on the entrance side at, e.g., $z = -a$. The similarity in the responses between the exit and entrance sides shows that the interference between the open and closed channels has a minor effect in the resonant en-
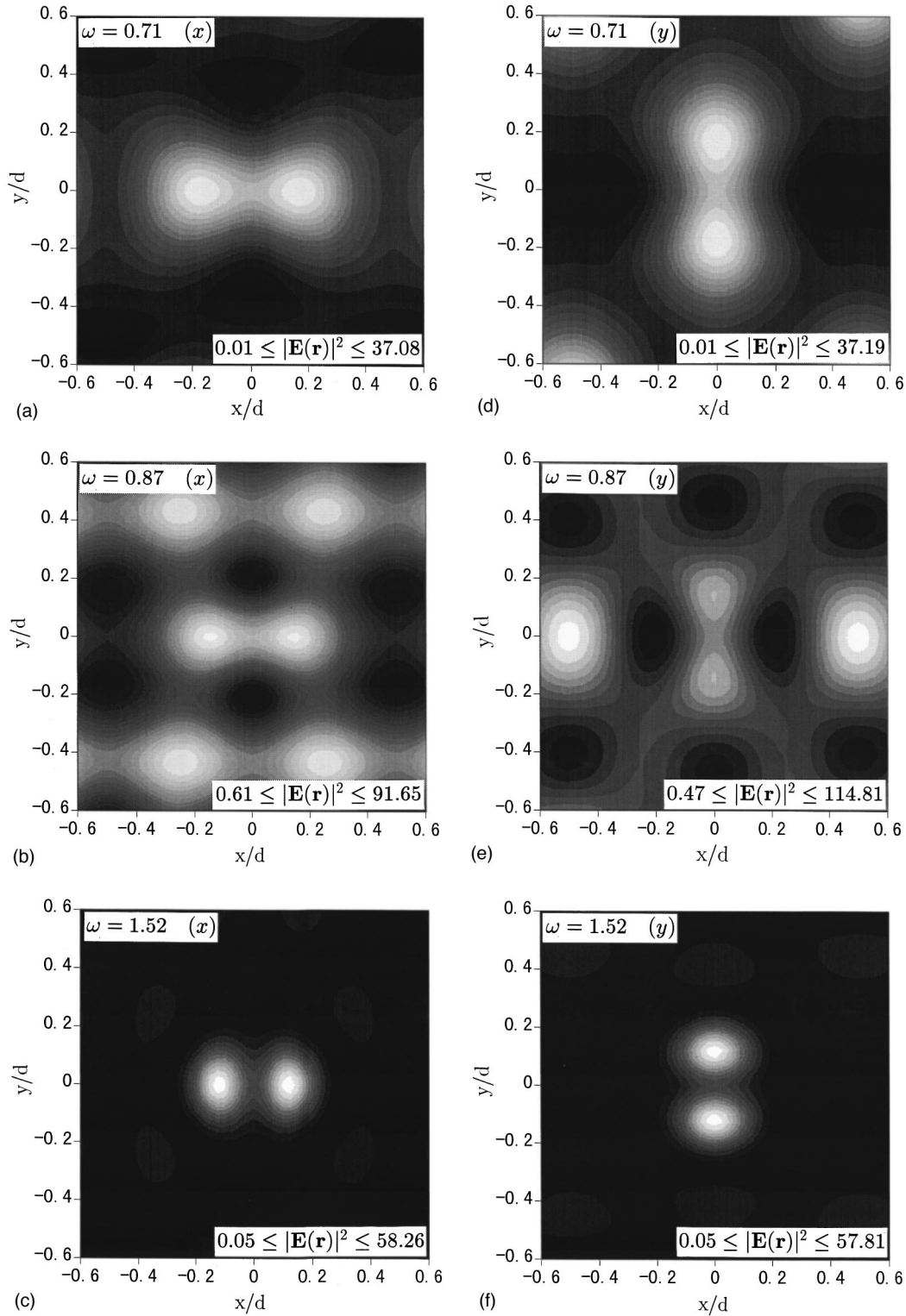
FIG. 4. Contour maps of the near-field intensity for the square region of Fig. 1. The intensity profiles are calculated on the sampling plane of $z=a$ at several resonances. The resonant frequencies are $\omega=0.71$ for (a) and (d), $\omega=0.87$ for (b) and (e), and $\omega=1.52$ for (c) and (f). The incident wave is taken to be p-polarized from (a) to (c) and to be s-polarized from (d) to (f).

hancement, because a peak of $\mathcal{R}$ on the entrance side must accompany the corresponding dip in $\mathcal{T}$ on the exit side.

We next examine the spatial dependence of the intensity, obtained at the frequency of just resonance. Figure 4 shows a map of the total electric-field intensity $|\mathbf{E}(\mathbf{r})|^2$ for p-

polarized incident field at $\mathbf{r}=(x,y,a)$, i.e., on the sampling plane at $z=a$. The panels (a)–(c) show the results at the resonances of Figs. 2 or 3, observed at $\omega=0.71$, 0.870, and 1.52, respectively. The results for the s incidence are given in (d)–(f). In the figures, x and y axes are scaled in units of d, so

that the tops of the spheres are located at (0,0), (1,0), (1/2,√3/2),... (see Fig. 1). The maximum and minimum values of the intensity are given in the panels.

It is interesting to note that none of the figures gives the brightest spot at the top of spheres, and that the contour maps are different for different resonances. Note that the field images of the s polarization in panels (d) and (f) are obtained basically from those of the p polarization by a $\pi/2$ rotation about the origin. Let us take a closer look at them.

In panel (a) for the p case of $\omega=0.71$, the contour looks like a lemniscate, while that of $\omega=1.52$ in (c) shows double-egg contour. A double-egg shaped contour is also observed in the resonance patterns of $\omega=0.857$ and 1.35 (not shown here). In contrast to (a) and (c), image (b) of $\omega=0.870$ shows a ladder with two maxima lying parallel to the x axis. Four secondary maxima are found at four of the six contact points of spheres. Two other contact points on the x axis remain dark. In the case of s polarization shown in (e), these two points are the maximum-intensity points. Secondary maxima of the s case are obtained by a $\pi/2$ rotation from the maximum points of the p case. From these observations it is found that the strict $\pi/2$ rotational symmetry between p and s does not exist. We can also guess that the bright spots of the near-field images for $\omega=0.870$ consist of two patterns, one attaining its maximum within each sphere and the other at the projected contact points. Whether a contact point turns out to be a bright spot or not depends on its local environment and the polarization of the incident field.

We next decompose the total field into its Cartesian components. Figures 5(a)–5(c) show, respectively, the x, y, and z components of the resonance pattern at $\omega=0.71$ and $z=a$ for p incidence. We see that $E_x(\mathbf{r})$ and $E_z(\mathbf{r})$ dominate in $|\mathbf{E}(\mathbf{r})|^2$ with negligible $E_y(\mathbf{r})$ contribution. E_x presents almost concentric circular contours in the central region, while E_z has a double peak along the x axis within a sphere. Therefore, we conclude that the two maxima of Fig. 4(a) is z-polarized and the region between them is x-polarized. This is, however, not always the case. In the case of $\omega=0.870$, for example, we find that three components are all appreciable [see Fig. 6(b) below].

The characteristic feature of the near-field images can be more directly analyzed by decomposing the total field into contributions from each channel. We introduce $E_i(\mathbf{h})$ for the transmitted field of channel $\mathbf{h}$ at height a:

$$E_i(\mathbf{h})=\sum_j T_{ij}(\mathbf{h0})\exp(i\mathbf{k_h^+}\cdot\mathbf{r_0})E_j^0, \qquad (3.2)$$

with $\mathbf{r_0}=(0,0,a)$. Then, the ith component of the outgoing field for $z>a$ is given by

$$E_i(\mathbf{r})=\sum_{\mathbf{h}} E_i(\mathbf{h})\exp[i\mathbf{k_h^+}\cdot(\mathbf{r}-\mathbf{r_0})]. \qquad (3.3)$$

Figure 6 displays complex amplitudes $E_i(\mathbf{h})$, with $i=x,y,z$ for several $\mathbf{h}$ for p incidence. The three panels (a), (b), and (c) correspond to $\omega=0.71$, 0.870, and 1.52, respectively. The arrows drawn from point $\mathbf{h}$ show the nonzero components of $[E_x(\mathbf{h}),E_y(\mathbf{h}),E_z(\mathbf{h})]$, whose real (imaginary) part is given by the horizontal (vertical) component of the respective arrows. Some points have an additional arrow that shows the z
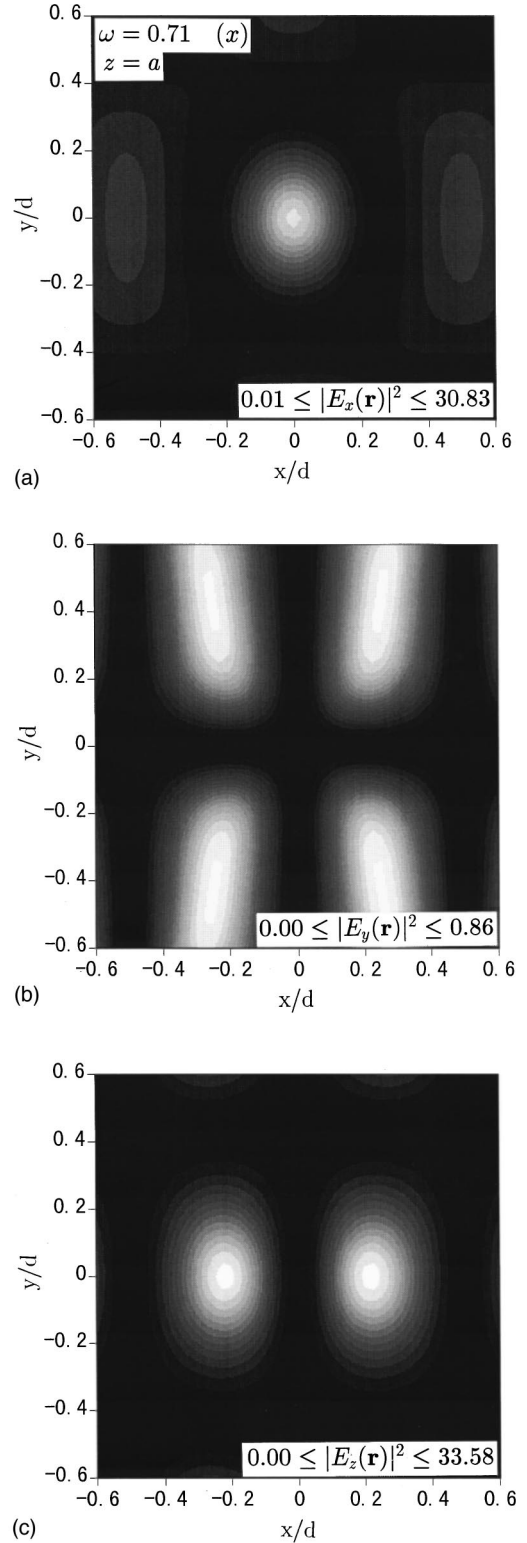
(a)

(b)

(c)

FIG. 5. Contour maps of the field components on the sampling plane at $z=a$. The panels (a), (b), and (c) show, respectively, $|E_x(\mathbf{r})|^2$, $|E_y(\mathbf{r})|^2$, and $|E_z(\mathbf{r})|^2$ with $\mathbf{r}=(x,y,a)$ for the p-polarized light of $\omega=0.71$.

component of s incidence (the x and y components of s incidence are obtained by the $\pi/2$ rotation of the p result).

For $\omega<1.0$, Figs. 6(a) and 6(b) show that appreciable amplitudes are seen only in the open channel $\mathbf{h}=0$ and the closed NN-shell channels. The field in the channel $\mathbf{h}=0$ has
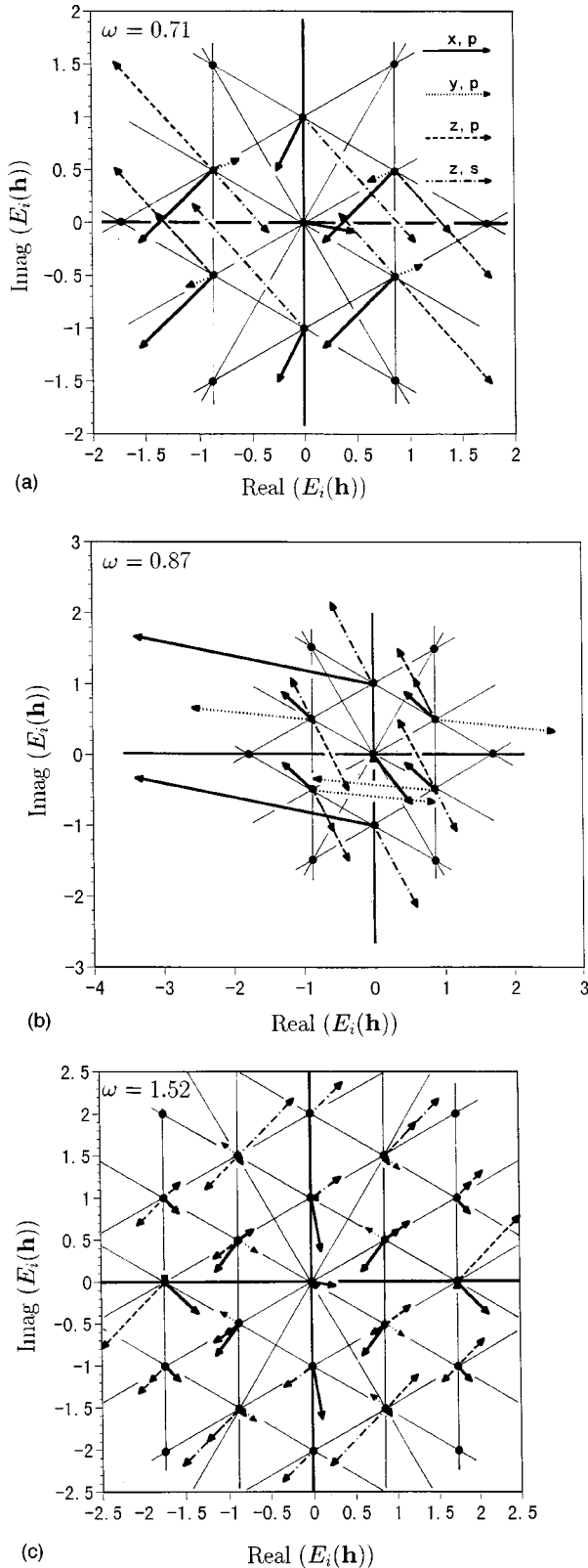
FIG. 6. Complex amplitudes $\mathbf{E}(\mathbf{h})$ for $\mathbf{h}=\mathbf{0}$ and several small $\mathbf{h}$. The frequencies are $\omega=0.71$ in (a), 0.870 in (b), and 1.52 in (c). The solid, dotted, and dashed lines, respectively, show the x, y, and z components of $\mathbf{E}(\mathbf{h})$ for the p-polarized light of normal incidence, while the dash-dotted line shows the z component of the s-polarized light. The components not shown are zero or negligibly small. Only in (c) are the amplitudes of 2NN and 3NN shells appreciable. The amplitudes 0 and NN shells are doubled in (c) as a guide to the eyes.

the same polarization as the incident light and determines the far-field intensity, i.e., $\mathcal{R}$ and $\mathcal{T}$ of Eq. (2.7). Panel (a) shows that at $\omega=0.71$ the NN-shell channels contribute mainly to the x and z components of the near field with negligible y component. In contrast, at the resonance of $\omega=0.870$ shown in (b), the y component is large. Thus, whether or not the y component is appreciable is the main origin for the difference in the two images. At $\omega=1.52$, panel (c) shows that the NN-shell channels, which are already open, have small amplitudes, their contribution to the near-field being accordingly minor. They in turn contribute to the far-field image, by giving rise to six diffracted waves. Then, the near-field images are mainly governed by the 2NN-shell channels, which are still closed.

The features of the NN-shell plane waves, seen commonly in the three panels of Fig. 6, are summarized as follows.

(i) Except for the two $\mathbf{h}$ on the k_y axis, points $\mathbf{h}_2$ and $\mathbf{h}_5$ of Fig. 1, $E_x(\mathbf{h})$'s are all directed in the same direction, showing that they are all in phase. The phases of $E_x(\mathbf{h}_2)$ and $E_x(\mathbf{h}_5)$ are identical but they are different from those of the remaining four $\mathbf{h}$.

(ii) $E_y(\mathbf{h})$'s always vanish at the points $\mathbf{h}_2$ and $\mathbf{h}_5$. Within any pair of $\mathbf{h}$ related by the mirror reflection in the xz or yz plane, $E_y(\mathbf{h})$'s are mutually out of phase by π.

(iii) $E_z(\mathbf{h})$'s also vanish at $\mathbf{h}_2$ and $\mathbf{h}_5$. For other $\mathbf{h}$ the arrows are mutually parallel (antiparallel) in a pair connected by the mirror reflection in the xz plane (yz plane).

The statement (i) explains the almost concentric circular contour of the $|E_x(\mathbf{r})|^2$ of Fig. 5(a), for it leads to the lateral dependence of the form $\cos h_x x \cos h_y y$, (h_x, h_y) being the lattice point in the first quadrant (point $\mathbf{h}_1$). The $\mathbf{h}_2$ and $\mathbf{h}_5$ on the y axis introduce a modification of the profile of $E_x(\mathbf{r})$, due to the $\cos h_y' y$ dependence, h_y' being the y component of $\mathbf{h}_2$. This modification is indeed seen in Fig. 5(a). From the statement (ii), which shows that the y component is expressed by $\sin h_x x \sin h_y y$, we can understand why the $E_y(\mathbf{r})$ vanishes on both x and y axes, as shown in Fig. 5(b). Likewise, the xy dependence of the form $\sin h_x x \cos h_y y$, deduced from the fact (iii), explains the presence of the double peak of Fig. 5(c).

The analysis for the s case is similarly possible. In the lateral components of electric field, p and s cases give an identical picture if we interchange the suffixes x and y. No such relation exists in the z component. The symmetry relations summarized above hold only for normal incidence and will be partly lost in the case of oblique incidence.

Finally, Fig. 7 shows the change of the near-field images with varying height of the sampling plane. Two cases of $z=1.2a$ and $2.0a$ for the resonances at $\omega=0.71$ and 1.52 of the p incidence are plotted. Panel (a) of $\omega=0.71$, as compared with Fig. 3(a), shows that a slight increase of z from a to $1.2a$ reduces the field intensity drastically without significantly modifying the field pattern. Since the maximum value of the intensity is roughly 4, the evanescent waves from the NN-shell channels are still the main origin of the intensity map. At $z=2a$ shown in panel (b), the evanescent waves are largely suppressed. Since channel $\mathbf{h}=\mathbf{0}$ cannot by itself produce the contrast, the contrast must be due to the interference between the plane wave of channel $\mathbf{h}=\mathbf{0}$ and the suppressed evanescent waves. Since the field in channel $\mathbf{h}=\mathbf{0}$ is x-
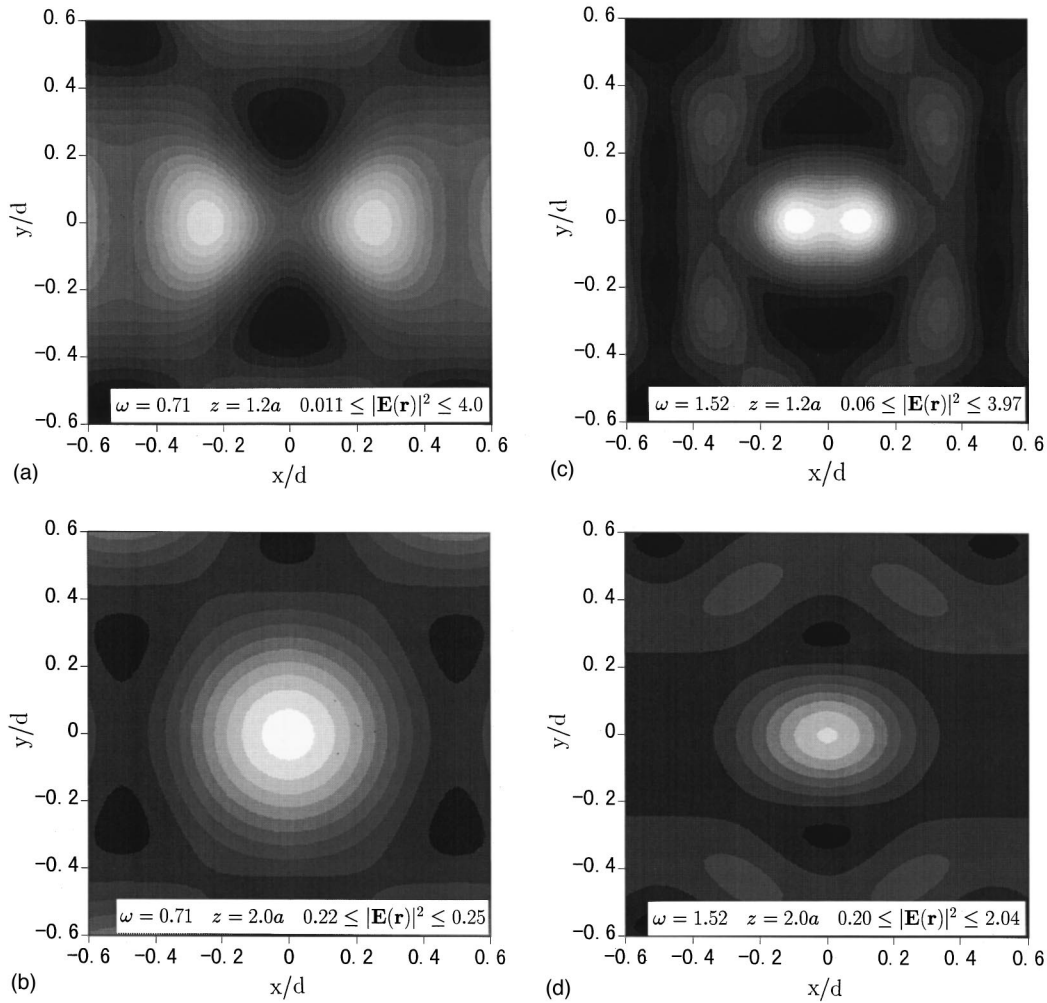
FIG. 7. Dependence of the near-field images on the distance of the sampling plane from the layer. The contour maps are given for $\omega = 0.71$. The panels (a) and (b) show the results on the sampling planes at $z=1.2a$ and $z=2.0a$, respectively. The contour maps for the frequency $\omega = 1.52$ are given in (c) and (d).

polarized, it will be the x component of the evanescent waves that interferes appreciably. The statement (i) above thus explains why the circular contrast of panel (b) is obtained. Note that the limiting value of the field intensity with increasing z tends precisely to that of the transmittivity $\mathcal{T}$, which is equal to $(1-\mathcal{R})$ when $\omega \lesssim 1.0$, $\mathcal{R}$ being shown in Fig. 2. The marked decrease of the peak intensity with higher z is also observed in the case of $\omega = 1.52$, as shown in Fig. 7(c). However, the maximum intensity remains rather large so that one can still observe a clear contrast even when $z=2a$, as shown in Fig. 7(d). These behaviors are natural consequences of the presence of the open NN-shell channels above $\omega = 1.0$.

B. Oblique incidence

We turn to the case of oblique incidence. Figure 8 shows $\mathcal{R}$ and the maximum field intensity at $\theta = 20°$ for the frequency range $\omega \lesssim 1.0$. The reflectivity is normalized by $\cos(\hat{\mathbf{k}}_0 \cdot \hat{\mathbf{z}})$ in accordance with Eq. (2.6), so that the unitarity condition of Eq. (2.6) turns out to be $\mathcal{T}+\mathcal{R}=1$. Below $\omega = 0.5$ the reflectivity has a single broad hump as in Fig. 2. Above $\omega = 0.5$, the spectra are very complicated. Between the reflectivity and the maximum field intensity, the peak

positions agree exactly. However, the peak positions of the responses to p and s lights are not identical, implying that the degeneracy seen in the case of normal incidence is lifted in the oblique incidence.

We give in Figs. 9(a) and 9(b) the near-field images of $\theta = 20°$ for p and s polarizations, respectively. The frequencies are chosen at the peak positions of $\omega = 0.73$ in (a) and 0.76 in (b). We obtain the images symmetric with respect to the x axis, but not to the y. This is a common feature of all the near-field images for the wave vector $\mathbf{k}_0$ lying in the xz plane. For the oblique incidence, we can check the following symmetry relations of the field components $i=x,y,z$:

$$E_i(\sigma_{vx}\mathbf{h}) = \pm E_i(\mathbf{h}), \tag{3.4}$$

where $\sigma_{vx}\mathbf{h}$ is the lattice point obtained from $\mathbf{h}$ by the mirror reflection in the xz plane. This is the origin for the symmetry of the intensity map with respect to the x axis.

C. Complex photonic bands of 2D system

The peaks of Fig. 8 occur due to the resonant excitation of photonic bands of the monolayer system. The photonic bands of the present system have 2D dispersion relations due to the
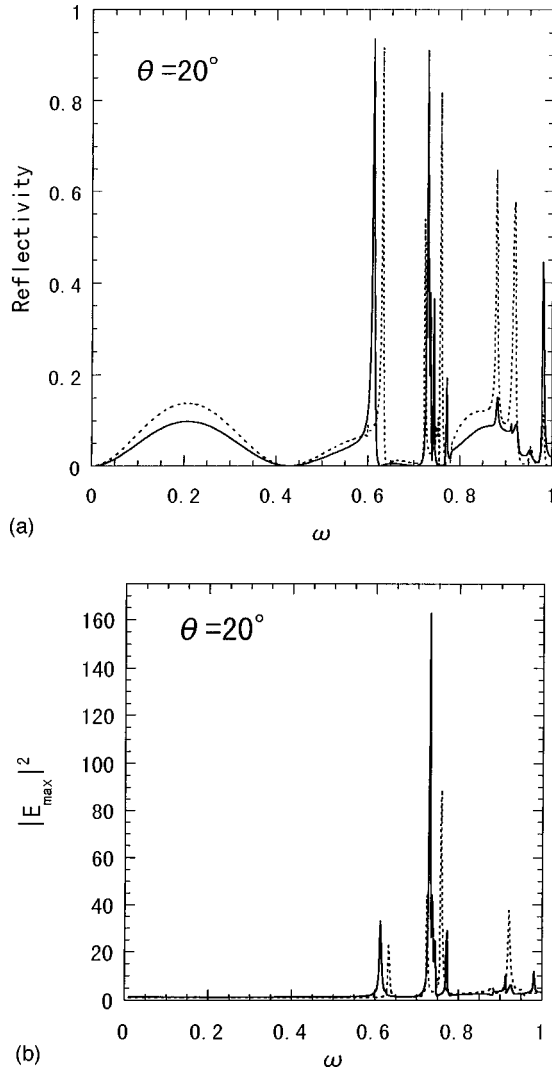
FIG. 8. Reflectivity $\mathcal{R}$ in (a) and maximum intensity of the local field on the plane at $z=a$ in (b). The incidence angle is $\theta=20°$. The solid and dotted lines show the results for the p and s lights, respectively.

translational symmetry in the lateral plane. Since their eigen-frequencies are in general complex, as stated in Sec. I, the derivation of the dispersion relation is not trivial.

Let us return to the reflection and transmission amplitudes given by Eq. (2.8). The central part of them is the layer t matrix $\tau^{\beta\beta'}$. When the determinant of the matrix **B** diverges somewhere in the complex ω plane in Eq. (2.10), so does $\tau^{\beta\beta'}$. The singularity is then transferred to the transmission and reflection coefficients through $T_{ii'}(\mathbf{hh'})$ and $R_{ii'}(\mathbf{hh'})$ of Eq. (2.8). Therefore, if we sweep ω along the real axis of the complex ω plane near some pole of det **B**, we obtain a Lorentzian resonance peak. The more the pole is located near the real axis, the sharper will be the line shape. If the effect of a pole of det **B** disappears in $T_{ii'}(\mathbf{hh'})$ or $R_{ii'}(\mathbf{hh'})$, the mode corresponding to the pole is optically inactive. This happens when the pole of det **B** fails to survive the procedure needed in Eqs. (2.9) and (2.8). Whether or not the pole has this property depends on the property of the eigenvector of matrix **B**, the information of which is carried by the residue of det **B** at that pole.
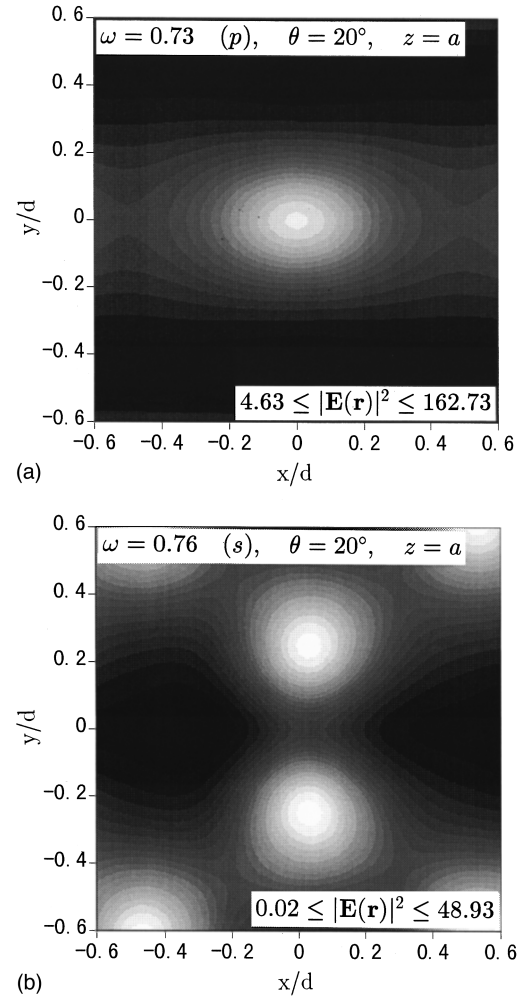

FIG. 9. Near-field images at $\theta=20°$ on the sampling plane at $z=a$; for the p light of $\omega=0.73$ in (a) and for the s light of $\omega=0.76$ in (b).

In Fig. 10 we plot $|\det \mathbf{B}|^2$ as a function of ω for oblique incidence. The result is given for $\theta=20°$ in the range $0.5 \leqslant \omega \leqslant 1.0$. We found that $|\det \mathbf{B}|^2$ turns out to be very spiky. Comparison of Fig. 10 with Fig. 8 shows that, wherever a peak occurs in $|\det \mathbf{B}|^2$, there is a corresponding sharp peak in both the reflectivity and the local field. This means that, if
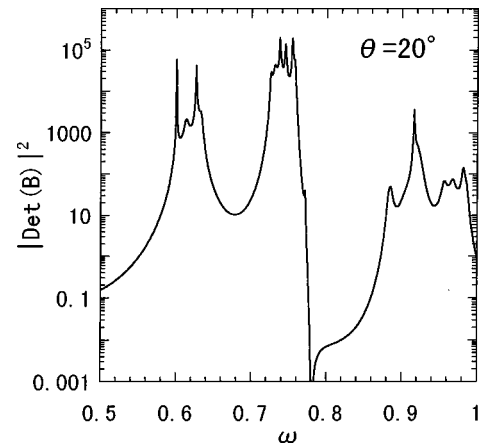

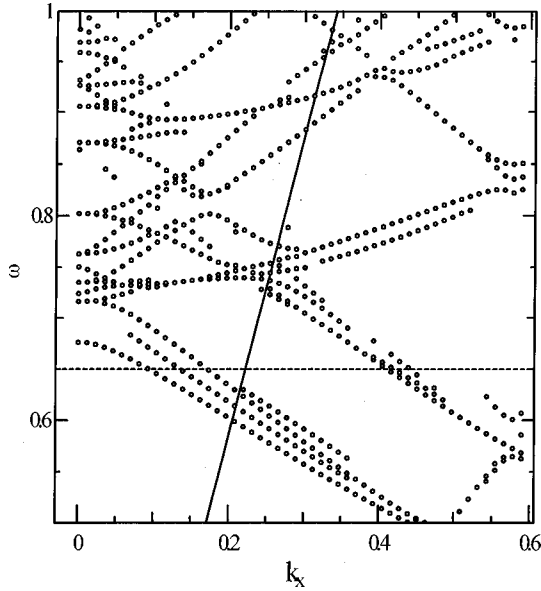FIG. 10. Plot of $|\det \mathbf{B}|^2$ for $\theta=20°$ as a function of ω.

FIG. 11. Dispersion relation for $\mathbf{k}=(k_x,0)$. The solid line is the $\omega-k_x$ line swept by the incident light with the incident angle fixed at $\theta=20°$. The horizontal dotted line is the one traced by the incident light of frequency $\omega=0.65$.

we use both s- and p-polarized lights, we can catch all the modes in the case of oblique incidence.

The dispersion relation of the photonic bands can be obtained by following the peak positions of $|\det \mathbf{B}|^2$. Figure 11 shows an example of the band structure of damped photonic bands, which is obtained for $\mathbf{k}=(k_x,0)$. Some of the dispersion curves disappear on the way. This implies that the corresponding peak gets blurred and leaves no trace as a well-defined peak in the plot of $|\det \mathbf{B}|^2$.

Calculating the local field with a fixed θ corresponds to tracing the optical response along the straight line $\omega=k_x/\sin\theta$ in the (k_x,ω) space, an example of which is drawn for the case of $\theta=20°$ in Fig. 11. Comparison of Fig. 11 with Fig. 2 reveals that there are many photonic bands, which are inactive at the Γ point to the incident light of normal incidence.

The procedure of varying θ with ω fixed is more easily carried out experimentally. The dotted horizontal line drawn at $\omega=0.65$ in Fig. 11 refers to this case. It crosses two bunches of bands. Figures 12(a) and 12(b) show, respectively, the reflectivity $\mathcal{R}$ and the near-field maximum-intensity as a function of θ for the same frequency as Fig. 11. We see two groups of peaks appear in the optical response in exact agreement with the positions of the band bunching. By comparing panel (b) with Fig. 11, we recognize that the missing parts of a band dispersion can be followed further by plotting the maximum intensity of the near field, because the well-defined peaks manifest themselves still in the ω dependence of the local field. The near-field information is thus more powerful in deriving the band dispersion than the far-field one.

In a series of panels (a)–(d) of Fig. 13, we show the change of the near-field images with varing θ.

IV. GROUP-THEORETICAL CONSIDERATION

The results of Sec. III C suggest that all the features related to the resonant frequency dependence will be explained
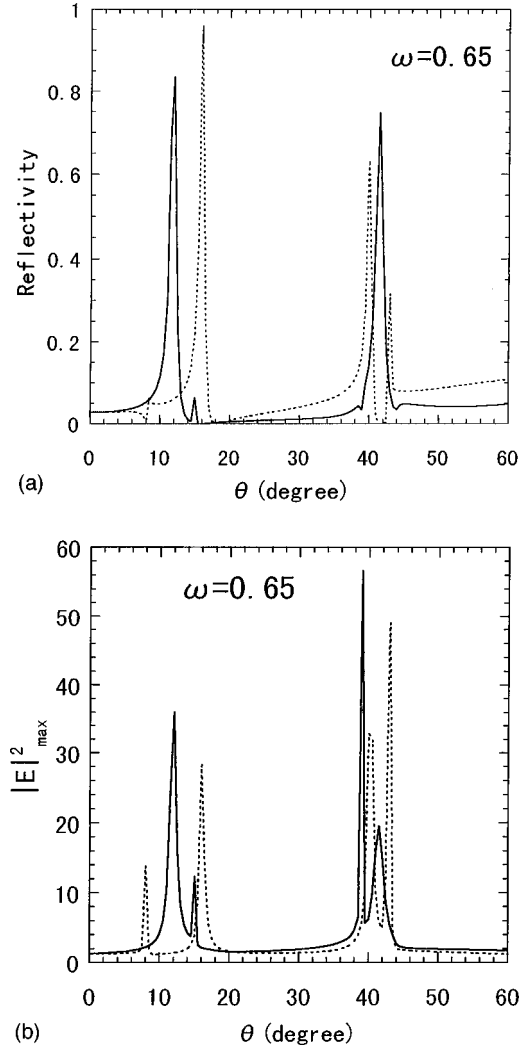

FIG. 12. Reflectivity $\mathcal{R}$ (a) and maximum intensity of the near-field images (b) as functions of θ. In (b) the field is calculated on the plane at $z=a$. The frequency is fixed at $\omega=0.65$. The solid and dotted lines show the cases of the p- and s-polarized lights, respectively.

by the properties of photonic bands excited optically. Therefore, we try in this section to interpret the calculated near-field profiles by using the group theory of a 2D photonic band.[25]

The photonic bands of the present system are classified according to the irreducible representation of $\mathcal{G}(\mathbf{k})$, the group of $\mathbf{k}$, for a 2D wave vector in the lateral plane. The electric field of each band has the following plane-wave representation of Bloch type:

$$\mathbf{E}_{\mathbf{k}}(\mathbf{r})=\sum_{\mathbf{h}}\mathbf{E}_{\mathbf{k}}(\mathbf{h})f_{\mathbf{k},\mathbf{h}}(z)\exp[i(\mathbf{k}+\mathbf{h})\cdot\boldsymbol{\rho}],\qquad(4.1)$$

for $\mathbf{r}=(\boldsymbol{\rho},z)$. The field variation with respect to z is described by the function $f_{\mathbf{k},\mathbf{h}}(z)$. The prefactors of the exponentials, including $f_{\mathbf{k},\mathbf{h}}(z)$, vary from band to band. Only when Eq. (4.1) of a band involves $e^{i\mathbf{k}\cdot\boldsymbol{\rho}}$, i.e., the term for the 0 shell, can that band be excited by a plane-wave light of wave vector $\mathbf{k}$. Thus, the condition that the 0-shell amplitude $\mathbf{E}_0(\mathbf{h}=0)$ is finite is the first requirement for a band to be excited optically.
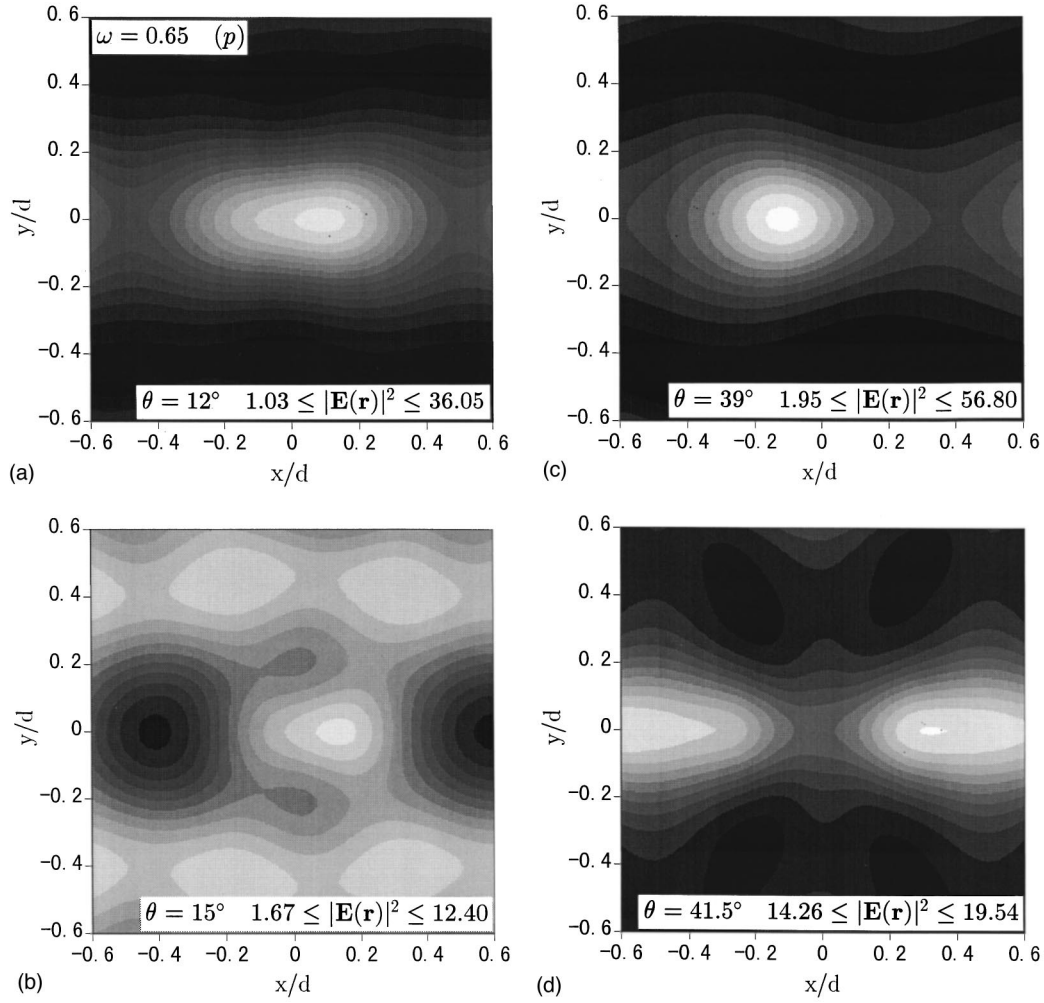
FIG. 13. Near-field images with varing θ. The sampling plane is at $z=a$ and the frequency is fixed at $\omega=0.65$ for the p polarization. The intensities are calculated at the peak positions of θ of Figs. 11; at $\theta=12°$ in (a), $15°$ in (b), $39°$ in (c), and $41.5°$ in (d).

In the case of the normal incidence, we set $\mathbf{k}=\mathbf{0}$. The point group of $\mathcal{G}(\mathbf{k}=\mathbf{0})$ is then C_{6v}, the symmetric group of a triangular lattice. The symmetry-adapted amplitudes $\mathbf{E_k}(\mathbf{h})$ of a band may be constructed by the standard procedure using the irreducible representation of that band. Namely, within each shell of equal $|\mathbf{h}|$, the $\mathbf{h}$ dependence of $\mathbf{E_{k=0}}(\mathbf{h})$ is wholly determined by the irreducible representation. Note that we may assign a single function $f_{\mathbf{k}=\mathbf{0},|\mathbf{h}|}(z)$ commonly to all $\mathbf{h}$ points within a shell.

The group C_{6v} has six irreducible representations,[25] four one-dimensional representations, A_1, A_2, B_1, B_2, and two two-dimensional ones, E_1 and E_2. As for the bands belonging to one-dimensional representations, the 0-shell amplitude $\mathbf{E_0}(\mathbf{h}=\mathbf{0})$ can be a basis function only if it is directed in the z direction. This is because it would otherwise rotate around the z axis by some operations of C_{6v} and cannot be a basis function by itself. A band whose $\mathbf{E_0}(\mathbf{h}=\mathbf{0})$ is z-directed belongs to A_1, the identity representation, since $\mathbf{E_0}(\mathbf{h}=\mathbf{0})$ is left unmoved under any operation of C_{6v}. Thus, all the one-dimensional irreducible representations except A_1 have zero $\mathbf{E_0}(\mathbf{h}=\mathbf{0})$. Also, A_1 bands are silent to the probe light of $\mathbf{k}=\mathbf{0}$, since the polarizations are mutually perpendicular. In conclusion, solely the doubly degenerate bands belonging to

E_1 and E_2 can be the candidates for the optically active bands. This was first shown by Stefanou et al.[26] and Robertson et al.[27]

Since the standard polynomial basis functions of E_1 and E_2 representations are $\{x,y\}$ and $\{xy,x^2-y^2\}$, respectively,[25] it is only the bands of E_1 symmetry that can be excited optically. E_2 bands fail to couple to any vector probe, because their basis functions transform like those of a second-rank tensor. This is another way of saying that an E_2 band cannot have a finite *vector*-amplitude $\mathbf{E_0}(\mathbf{h}=\mathbf{0})$. The conclusion for the case of $\mathbf{k}=\mathbf{0}$ is thus that an incident light can excite only the bands of E_1 representation. Thus, all the resonance excitations of photonic bands should be identical as far as the group-theoretical properties are concerned. Since the electric fields of E_1 bands transform like x and y, one of the twofold degenerate bands may be excited by the p-polarized light and its partner by the s light. In spite of this simple conclusion, however, the intensity profiles seen in Sec. III varied rather strongly depending on the resonance.

In the NN shell, we have 18 vector plane waves of the form $\exp(i\mathbf{h}\cdot\mathbf{r})$: each of the six points in the NN shell has three vectors, polarized in the x, y, and z directions. These 18 vectors form a (reducible) representation of C_{6v} of dimen-

sion 18×18. We find that its irreducible decomposition is $2A_1 + A_2 + B_1 + 2B_2 + 3E_1 + 3E_2$.

Figure 14 lists their basis functions, including those of the optical inactive E_2 and one-dimensional representations. In the column NN, the basis functions constructed by superposing the 18 plane waves are shown. The column 2NN involves those arising from 2NN shell. Two basis functions of E_1 representation are denoted by E_{11} and E_{12}, E_{11} transforming like x (active to the p light), and E_{12} like y (active to the s). The basis functions in the column z are the ones constructed by superposing the z-directed vector plane waves and hence polarized in the z direction. The columns σ and π show the basis functions polarized in the lateral plane, the σ basis being directed in the radial direction and π in the direction perpendicular to it.

Correspondingly, any band of E_1 representation is an admixture of the three types of the basis vectors, z, σ, and π.

The diversity of the near-field images should arise depending on how these three types are mixed.

Decomposing $\mathbf{E}_0(\mathbf{h})$ into z, σ, and π basis functions is not possible by the symmetry consideration. It is only fixed by the eigenvector of the matrix $\mathbf{B}$ of Eq. (2.10). We avoid the time-consuming numerical task of searching complex eigenvalues of the matrix $\mathbf{B}$ and calculating their eigenvectors. Instead, by assuming how the three types are mixed, we shall attempt an analytical construction of the near-field images.

Let us consider the images shown in Figs. 4(a) and 4(b). Since they are the images of p light, we need to consider only the basis functions E_{11}. We restrict ourselves to the contribution of the NN shell. Let us denote the three types of the symmetry-adapted basis functions as $\mathbf{E}_{11}^z(\boldsymbol{\rho})$, $\mathbf{E}_{11}^\sigma(\boldsymbol{\rho})$, and $\mathbf{E}_{11}^\pi(\boldsymbol{\rho})$. Introducing three mixing parameters, C^z, C^σ, and C^π, we find from Table I that the electric field yielded by them has the form

$$\mathbf{E}_{\mathbf{k}=0}(\mathbf{r}) = C^\sigma \mathbf{E}_{11}^\sigma(\boldsymbol{\rho}) + C^\pi \mathbf{E}_{11}^\pi(\boldsymbol{\rho}) + C^z \mathbf{E}_{11}^z(\boldsymbol{\rho}) = \begin{cases} (2\sqrt{3}C^\sigma + 2C^\pi)\cos h_x x \cos h_y y + 4C^\pi \cos h_y' y & \text{for } E_x \\ (-2C^\sigma + 2\sqrt{3}C^\pi)\sin h_x x \sin h_y y & \text{for } E_y \\ 4iC^z \sin h_x x \cos h_y y & \text{for } E_z, \end{cases} \tag{4.2}$$

with

$$h_x = \frac{2\pi}{d}, \quad h_y = \frac{1}{\sqrt{3}}\frac{2\pi}{d}, \quad h_y' = \frac{2}{\sqrt{3}}\frac{2\pi}{d}. \tag{4.3}$$

The quantities h_x and h_y define the six points of the NN shell. Here $f_{\mathbf{k}=0,|\mathbf{h}|}(z)$ of Eq. (4.1) is dropped for brevity. The exact form of $\mathbf{E}_{\mathbf{k}=0}(\mathbf{r})$ must include the contributions of all shells, open or closed. By Eq. (4.3), we are examining to what extent the NN-shell contribution explains Figs. 4(a) and 4(b).

Of the three Cartesian components of $\mathbf{E}_{\mathbf{k}=0}(\mathbf{r})$, the z component comes only from the basis $\mathbf{E}_{11}^z(\mathbf{r})$. We can easily see that the symmetry properties summarized in the statement (iii) of Sec. III A is actually realized in the z component of Eq. (4.2). The same holds true for the x and y components. Especially, the statement (i) made for the $E_x(\mathbf{h}_2)$ and $E_x(\mathbf{h}_5)$ for the lattice points on the k_y axis holds because of the second term of the x component of Eq. (4.2), which comes from the π basis. Also, whether or not the y component is appreciable—the main reason for the difference of Figs. 4(a) and 4(b)—depends on the relative signs of the mixing coefficients C^σ and C^π. If they are of the same sign, the near-field image similar to panel (a) of Fig. 4 will result, while the profile like panel (b) will be obtained, if they are of opposite sign.

Indeed, Fig. 15 shows the intensity map of $|\mathbf{E}(\mathbf{r})|^2$, for one choice $C^\sigma = 0.7$, $C^\pi = 0.1$, and $C^z = 0.9$ in panel (a) and for another choice $C^\sigma = 0.5$, $C^\pi = -1.5$, and $C^z = 0.5$ in panel (b), together with their bird's-eye views. We took the mixing coefficients as real and fixed their magnitudes arbitrarily except for the relative signs of C^π and C^σ. By inspection, we readily recognize that the numerical results are re-

produced quite satisfactorily by the analytical expression. Since we have plotted only the absolute square of the NN contribution, the agreement implies that the interference between the open 0-channel and the closed NN-channels is not important very near the system. Also, the fact that the coefficients C^σ, etc. are actually complex, is not very important.[28]

The fact that the NN shell is dominant is reasonable, since it contributes most of all to the evanescent field, and hence to the near field. For a sampling plane positioned farther away from the array of spheres, the NN contribution decreases exponentially with the result that the 0-shell contribution and the interference between the 0- and NN-NN shells become important, relative to the absolute square of the NN contribution considered above. Also, when ω is larger than 1.0, the contribution from the 2NN shell must be taken into account. These statements are all in accord with what has been mentioned for Fig. 6.

The case of the s incidence is similarly analyzed by using the basis functions of E_{12}. Without repeating the analysis, we point out only one thing in relation to the p case. When we return to Table I and compare E_{12} with E_{11}, we see that their σ and π basis functions are related by the $\pi/2$ rotation around the z axis (this may be more easily seen in Fig. 14). For example, the change $x \to y$ and $y \to -x$ alters the σ (π) basis of E_{11} to the π (σ) of E_{12}. These properties between E_{11} and E_{12} are observed similarly in the 2NN channels, as Table II shows. This is the reason for the $\pi/2$ rotational symmetry between the lateral components of the p and s results. The z component has no such symmetry, as Table I shows. These explain just what we have observed in Fig. 4.

For the oblique incidence of $\mathbf{k}$ lying in the xz plane, the point group of $\mathcal{G}(\mathbf{k})$ is C_{1h}, composed of the identity operation and the mirror reflection in the xz plane. The point group

(a)

(b)

(c)

FIG. 14. Display of the basis functions of the irreducible representations of C_{6v}. Panels (a) and (b) show the basis functions of E_1 and E_2, respectively. An arrow given the number 2 is twice as long as the other arrows. In the column z, the circles show the polarizations directed in the $+z$ direction, while the crosses show them in the $-z$ direction. In the diagram of (NN, π) of (a), the basis function of $\mathbf{h}=\mathbf{0}$ is given. The panel (c) shows the basis functions of one-dimensional representations.

C_{1h} has two one-dimensional irreducible representations A' and A'', which are, respectively, even and odd with respect to the mirror reflection in the xz plane. Thus, the 2D bands of symmetry A' are active to the p light, which is polarized in the xz plane, and the bands of A'' to the s light. Namely, any band is active optically in the oblique case. Combination of a lattice point $\mathbf{h}=(h_x,h_y)$ with its mirror-reflected partner $(h_x,-h_y)$ yields the electric field of the form $e^{ih_xx}\sin h_yy$ or $e^{ih_xx}\cos h_yy$, depending on which of A' and A'' the band belongs to. This is the origin of the mirror symmetry of the field with respect to the x axis, summarized by Eq. (3.4). There is no other symmetry in the oblique case.

V. NEAR-FIELD IMAGE FOR SMALL ω

When the incident wavelength is orders of magnitudes larger than the size of the spheres, one might expect the near-field image to be uniform without any observable contrast. However, this is not the case. Figure 16 shows the near-field images at $\omega=0.02$, the wavelength λ being $50\sqrt{3}$ times larger than the sphere radius a [see Eq. (3.1)]. Panel (a) is given for the case of the p-polarized light of $\theta=0$, (b) for (p, $\theta=80°$), and (c) for (s, $\theta=0$). The sampling plane is chosen at $z=a$. These panels show definitely that a contrast does exist within a sphere.

Let us summarize the main features of Fig. 16. From (a), we see that the near-field image of the normally incident p light is a negative image of the real lattice of spheres, taking the minimum intensity at the center and the maximum at the contact points $\boldsymbol{\rho}=(\pm a,0)$ on the x axis. When θ increases, the maximum position moves towards the center, as shown in (b). In contrast, the profile of s light given in (c) has the bright lines parallel to the x axis in the neighborhood of the line $y=\pm(\sqrt{3}/4)d$. Also, the s profile is almost independent of θ [so that we have not given the result for the case of (s, $\theta=80°$)]. These characteristics for both polarizations persist irrespective of ω.

In the long wavelength limit, each of the spheres is regarded as a point electric dipole of dipole moment $\mathbf{p}$. For the exciting light of frequency ω with amplitude $\mathbf{E}^0$ of unit strength, the induced moment is given by

$$\mathbf{p}=a^3\frac{\varepsilon-1}{\varepsilon+2}\mathbf{E}^0\equiv\alpha\mathbf{E}^0 \qquad (5.1)$$

with ε the dielectric constant of the spheres and α the polarizability. Our task is to calculate the scattered electric field from a 2D periodic array of point dipoles.

The Hertz vector at $\mathbf{r}=(\boldsymbol{\rho},z)$ of the induced dipole moment located at $\mathbf{r}_d=(\boldsymbol{\rho}_d,0)$ on the xy plane is given by

$$\boldsymbol{\Pi}(\mathbf{r})=\mathbf{p}\exp(i\mathbf{k}\cdot\boldsymbol{\rho}_d)\frac{\exp(i\omega|\mathbf{r}-\mathbf{r}_d|)}{|\mathbf{r}-\mathbf{r}_d|}, \qquad (5.2)$$

where the phase of the incident wave at $\mathbf{r_d}$ is taken into account in terms of $\mathbf{k}$, the lateral component of the incident wave vector. Fourier transform of the outgoing wave from $\mathbf{r_d}$ is

$$\frac{\exp(i\omega|\mathbf{r}-\mathbf{r}_d|)}{|\mathbf{r}-\mathbf{r}_d|}$$
$$=2\pi i\int\frac{d\mathbf{q}}{(2\pi)^2}\frac{\exp\{i\mathbf{q}\cdot(\boldsymbol{\rho}-\boldsymbol{\rho}_d)+i\gamma(\mathbf{q})^{\pm}z\}}{\gamma(\mathbf{q})^+}, \qquad (5.3)$$

with $\gamma(\mathbf{q})^{\pm}=\pm(\omega^2-\mathbf{q}^2)^{1/2}$ and the superscript $+$ ($-$) given for positive (negative) z. Therefore, the total Hertz vector of the 2D periodic array is given by

$$\boldsymbol{\Pi}(\mathbf{r})=\mathbf{p}\sum_{\boldsymbol{\rho}_d}\exp(i\mathbf{k}\cdot\boldsymbol{\rho}_d)2\pi i$$
$$\times\int\frac{d\mathbf{q}}{(2\pi)^2}\frac{\exp\{i\mathbf{q}\cdot(\boldsymbol{\rho}-\boldsymbol{\rho}_d)+i\gamma(\mathbf{q})^{\pm}z\}}{\gamma(\mathbf{q})^+}. \qquad (5.4)$$

The integral over $\mathbf{q}$ is carried out by using

TABLE I. Dependence on $\boldsymbol{\rho}=(x,y)$ of the electric field expressed by the basis functions E_{11} and E_{12} for $\mathbf{h}$ in the NN shell. Three types of the basis functions are shown in Fig. 16. The components not shown are zero. In this table, $h_x=2\pi/d$, $h_y=2\pi/(\sqrt{3}d)$, and $h'_y=4\pi/(\sqrt{3}d)$.

	NN		
	z	σ	π
E_{11}	$E_z=4i\,\sin h_x x\,\cos h_y y$	$E_x=2\sqrt{3}\,\cos h_x x\,\cos h_y y$ $E_y=-2\,\sin h_x x\,\sin h_y y$	$E_x=2\,\cos h_x x\,\cos h_y y$ $+4\,\cos h'_y y$ $E_y=2\sqrt{3}\,\sin h_x x\,\sin h_y y$
E_{12}	$E_z=-4i\,\cos h_x x\,\sin h_y y$ $+4i\,\sin h'_y y$	$E_x=-2\sqrt{3}\,\sin h_x x\,\sin h_y y$ $E_y=2\,\cos h_x x\,\cos h_y y$ $+4\,\cos h'_y y$	$E_x=2\,\sin h_x x\,\sin h_y y$ $E_y=2\sqrt{3}\,\cos h_x x\,\cos h_y y$

$$\sum_{\boldsymbol{\rho}_d}\exp[-i\boldsymbol{\rho}_d\cdot(\mathbf{q}-\mathbf{k})]=\frac{(2\pi)^2}{S}\sum_{\mathbf{h}}\delta(\mathbf{q}-\mathbf{k}-\mathbf{h}), \quad (5.5)$$

S being the area of the unit cell. Once the total Hertz vector is obtained, operating $(\omega^2+\nabla\nabla)$ yields the scattered electric field $\mathbf{E}_s(\mathbf{r})$. The result is[29]

$$\mathbf{E}_s(\mathbf{r})=\frac{2\pi i}{S}\sum_{\mathbf{h}}\frac{\omega^2\mathbf{p}-\mathbf{k}_{\mathbf{h}}^{\pm}(\mathbf{k}_{\mathbf{h}}^{\pm}\cdot\mathbf{p})}{\Gamma_{\mathbf{h}}^{+}}\exp(i\mathbf{k}_{\mathbf{h}}^{\pm}\cdot\mathbf{r}), \quad (5.6)$$

where $\mathbf{k}_{\mathbf{h}}=(\mathbf{k}+\mathbf{h},\Gamma_{\mathbf{h}}^{\pm})$ with $\Gamma_{\mathbf{h}}^{+}=\gamma(\mathbf{k}+\mathbf{h})^{+}$ introduced in Eq. (2.3). The local field at the position $\mathbf{r}$ is given by Eq. (5.6) plus the incident plane wave $\mathbf{E}^0\exp(i\mathbf{k}\cdot\boldsymbol{\rho}+i\Gamma_0^{+}z)$.
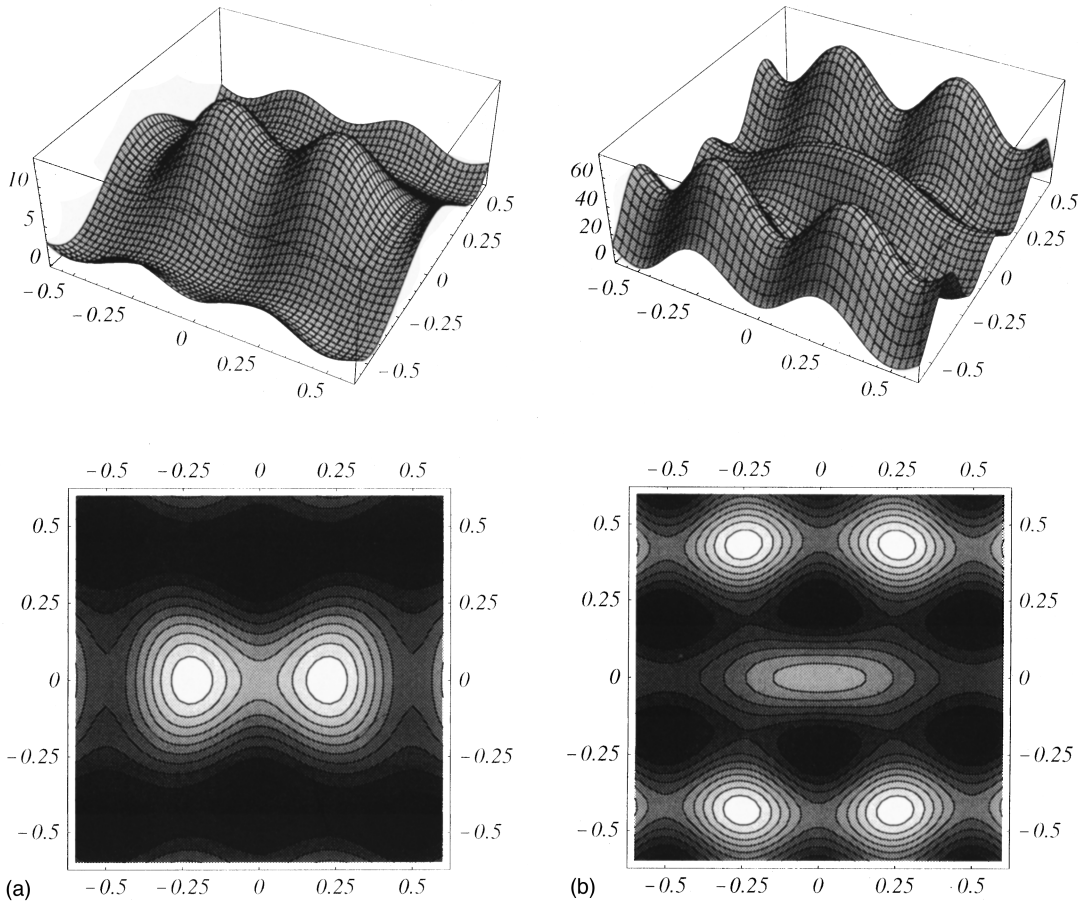

FIG. 15. Analytical intensity map for Figs. 4(a) and 4(b). The intensity of the field given by Eq. (4.2) is shown with their bird's-eye views. The values of the mixing parameters C^{σ}, etc., for the two panels are given in the text. Two panels (a) and (b) correspond, respectively, to Figs. 4(a) and 4(b).
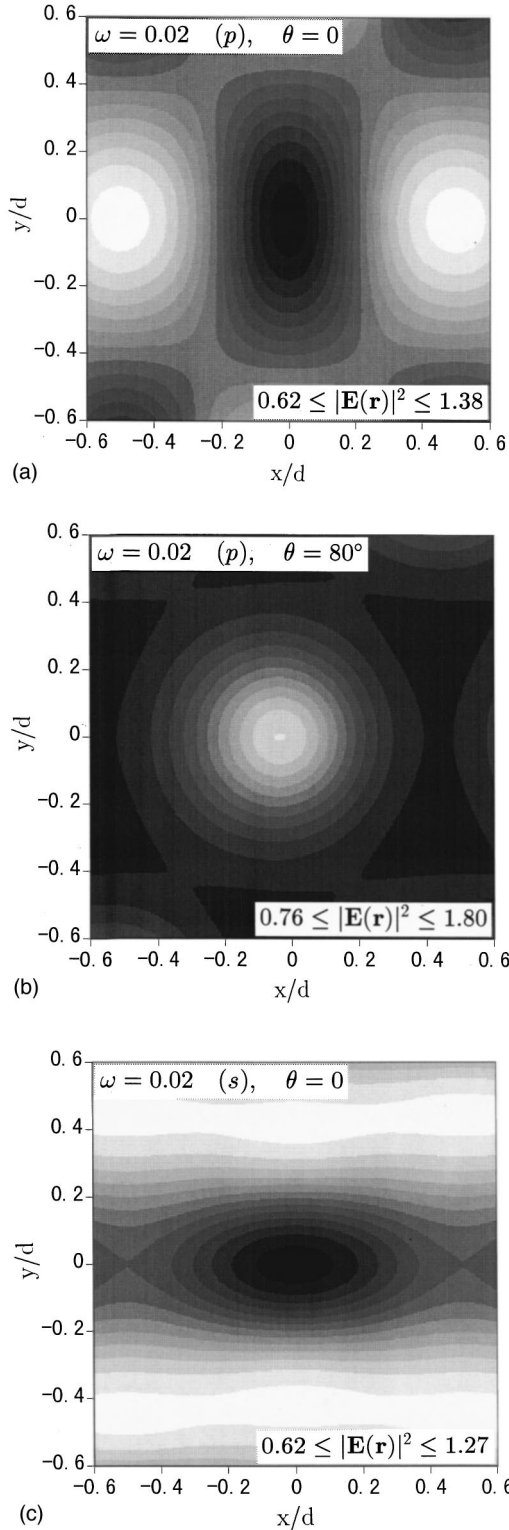
(a)

(b)

(c)

FIG. 16. Near-field images in the long wavelength limit. The intensity profile on the sampling plane at $z=a$ is shown for the p-polarized light of $\omega=0.02$; for $\theta=0$ in (a) and for $\theta=80°$ in (b). Panel (c) shows it for the s light of $\theta=0$.

Let us analyze Eq. (5.6) in the limit $\omega\to0$, where only the channel $\mathbf{h}=0$ is open. We begin by the far field.

A. Intensity of the far field

In the expression of the far field, all the terms except $\mathbf{h}=\mathbf{0}$ decay out. In the normal incidence ($\mathbf{k}=\mathbf{0}$ and $\mathbf{E^0}$ in the
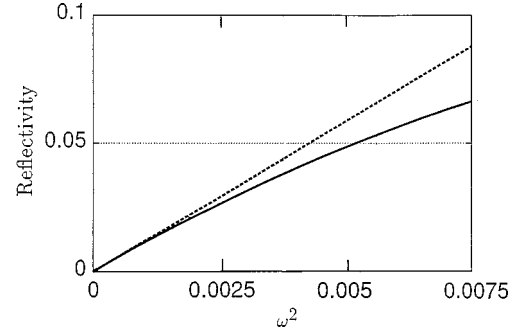

FIG. 17. Reflectivity $\mathcal{R}$ in the long wavelength limit (solid curve). The horizontal axis is ω^2. The data of Fig. 2 are used.

xy plane), we have accordingly $\mathbf{k}^{\pm}_{\mathbf{h}=0}=(0,0,\Gamma^{\pm}_{\mathbf{h}=0})=(0,0,\pm\omega)$. Since $\mathbf{p}\|\mathbf{E^0}$ from Eq. (5.1), the inner product $\mathbf{k}^{\pm}_{\mathbf{h}}\cdot\mathbf{p}$ vanishes in Eq. (5.6), leading to

$$\mathbf{E}_s(\mathbf{r})=\frac{2\pi i}{S}\,\alpha\omega\,\exp(\pm i\omega z)\mathbf{E^0}. \qquad (5.7)$$

This gives ω^2 dependence of the reflectivity $\mathcal{R}$. This is a remarkable feature of the light scattering from a 2D periodicity, to be compared with the familiar ω^4 law of the Rayleigh scattering. Figure 17 reproduces the long wavelength part of $\mathcal{R}$ of Fig. 2 as a function of ω^2. The result supports clearly the present analysis.

Equation (5.6) is similarly analyzed in the case of oblique incidence. We find that the intensity of $\mathbf{E}_s(\mathbf{r})$ remains unaltered apart from the θ dependence of the p case, described by the factor $\cos^2 2\theta/\cos^2\theta$.

B. Intensity profile of near field

In the near-field expression, the term involving $\mathbf{k}^{\pm}_{\mathbf{h}}\cdot\mathbf{p}$ is dominant in Eq. (5.6). Since the exponential decay in the z direction is determined by $\pm|\Gamma_{\mathbf{h}}|$, it suffices to consider only the NN shell in the sum over $\mathbf{h}$. In addition, one may neglect $\mathbf{k}$ in $\mathbf{k}^{+}_{\mathbf{h}}$ and ω in $\Gamma^{+}_{\mathbf{h}}$, so that $\Gamma^{+}_{\mathbf{h}}\cong i|\mathbf{h}|$ and $\mathbf{k}^{+}_{\mathbf{h}}\cong(\mathbf{h},i|\mathbf{h}|)$ with $|\mathbf{h}|=4\pi/\sqrt{3}d$, the radius of the NN shell.

We begin by the simpler case of s incidence, where the dipole moment $\mathbf{p}$ is induced in the y direction, leading to $\mathbf{k}^{+}_{\mathbf{h}}\cdot\mathbf{p}=\alpha(\mathbf{h})_y$. In the near-field intensity, the cross term $\mathbf{E_0}(\mathbf{r})^*\cdot\mathbf{E}_s(\mathbf{r})$ between the incident and scattered fields is the main origin of the contrast, because $|\mathbf{E}_s(\mathbf{r})|^2$ is much smaller in comparison [for the magnitudes of $\mathbf{E}_s(\mathbf{r})$, see the comment given in Ref. 30]. In the s incidence ($\mathbf{E_0}$ is directed in the y direction), the y component of $\mathbf{E}_s(\mathbf{r})$ enters in the cross term, which is written at $z=a$ as

$$(\mathbf{E}_s)_y=-\frac{2\pi\alpha}{S}\frac{\exp(-|\mathbf{h}|a)}{|\mathbf{h}|}\sum_{\mathbf{h}''}(\mathbf{h}''_y)^2\exp(i\mathbf{h}''\cdot\boldsymbol{\rho})$$

$$=-f_y4h_y^2(\cos h_x x\,\cos h_y y+2\,\cos h'_y y), \qquad (5.8)$$

with $f_y=2\pi\alpha e^{-|\mathbf{h}|a}/(S|\mathbf{h}|)$ and the values of h_x, etc. being given by Eq. (4.3). Here the second line is the result of the sum over six $\mathbf{h}''$ points in the NN shell. From this expression we find that $(\mathbf{E}_s)_y$ is real and that it takes the negative minimum value at the top of sphere [$(x,y)=(0,0)$] and the positive maximum on the lines $y=\pm(\sqrt{3}/4)d$, where $h_y y=\pi/2$

TABLE II. Dependence on $\boldsymbol{\rho}=(x,y)$ of the electric field of the basis functions E_{11} and E_{12} for $\mathbf{h}$ in the 2NN shell. The components not shown are zero. In this table, $h_x=2\pi/d$, $h_y=2\sqrt{3}\pi/(d)$, and $h_x'=4\pi/(d)$.

		2NN	
	z	σ	π
E_{11}	$E_z=4i\ \sin h_x x \cos h_y y$ $+4i\ \sin h_x'x$	$E_x=2\cos h_x x \cos h_y y$ $+4\cos h_x'x$ $E_y=-2\sqrt{3}\ \sin h_x x \sin h_y y$	$E_x=2\sqrt{3}\ \cos h_x x \cos h_y y$ $E_y=2\sin h_x x \sin h_y y$
E_{12}	$E_z=-4i\ \cos h_x x \sin h_y y$	$E_x=-2\sin h_x x \sin h_y y$ $E_y=2\sqrt{3}\ \cos h_x x \cos h_y y$	$E_x=2\sqrt{3}\ \sin h_x x \sin h_y y$ $E_y=\cos h_x x \cos h_y y$ $+4\cos h_x'x$

and $h_y'y=\pi$. These two lines connect the contact points of the spheres parallel to the x axis. In addition, the contribution is independent of θ. These are just the features of Fig. 16, summarized above for the s incidence.

As for the intensity, $0.62<|\mathbf{E}(\mathbf{r})|^2<1.27$ is the exact numerical result of the case of $\varepsilon=1.6^2$, as marked in Fig. 16(c), while the intensity due to Eq. (5.8) plus the incident field is $0.67<|\mathbf{E}(\mathbf{r})_y|^2<1.25$. The similarity of the upper and lower bounds confirms the correctness of the present analysis. The slight discrepancy will be attributed partly to the presence of the components other than y and partly to the ω dependence neglected in Eq. (5.8).

In striking contrast to the case of s polarization, a marked θ dependence is obtained in the p case. In the perpendicular ($E_x^0=1.0$) and grazing incidences ($E_z^0=-1.0$) of the p light, the dipole moment $\mathbf{p}$ is induced in the x and z directions, respectively. It is then easy to see that $\mathbf{E}_s$ is x-directed when $\theta\simeq0$ and z-directed when $\theta\simeq\pi/2$:

$$(\mathbf{E}_s)_x=-\frac{2\pi\alpha}{S}\frac{\exp(-|\mathbf{h}|a)}{|\mathbf{h}|}\sum_{\mathbf{h}''}(h_x'')^2\exp(i\mathbf{h}''\cdot\boldsymbol{\rho})$$
$$=-f_x4h_x^2\cos h_x x \cos h_y y\quad\text{for }\theta\cong0,$$
(5.9)
$$(\mathbf{E}_s)_z=-\frac{2\pi\alpha}{S}|\mathbf{h}|\exp(-|\mathbf{h}|a)\sum_{\mathbf{h}''}\ \exp(i\mathbf{h}''\cdot\boldsymbol{\rho})$$
$$=-f_z4h_x^2\left(\cosh_x x \cos h_y y+\frac{1}{2}\cos h_y'y\right)\quad\text{for }\theta\simeq\frac{\pi}{2},$$

with $f_x=f_y$ and $f_z=\frac{4}{3}f_y$, f_y being defined below Eq. (5.8). In the normal incidence, therefore, $(\mathbf{E}_s)_x$ gives the positive maximum at the contact point of the spheres on the x axis and the negative minimum at $x=y=0$. For $\theta\cong\pi/2$, $(\mathbf{E}_s)_z$ has the negative maximum at the top of the spheres. Thus, the inner product $\mathbf{E_0}(\mathbf{r})^*\cdot\mathbf{E}_s(\mathbf{r})$ reproduces the near-field images of the p-polarized case shown in Figs. 16(a) and 16(b).

Note that for both p and s cases, the above features of (x,y) dependence are independent of ε and a, for they enter only through the polarizability α defined by Eq. (5.1).

Also, if we assume α to be ω-independent, so are both $\mathbf{E}_s$ and $\mathbf{E_0}(\mathbf{r})^*\cdot\mathbf{E}_s(\mathbf{r})$. This leads to the important conclusion that the near-field image is, in magnitudes as well as in shape of the contour, independent of ω in the long wavelength limit. We have checked this fact by repeating the calculation for $\omega=0.002$ and confirmed that the result is in fact the same as Fig. 16.

The key to the fine resolution in spite of the very long wavelength of light is the phase involved in $\exp[i(\mathbf{k}+\mathbf{h})\cdot\boldsymbol{\rho}]$ of Eq. (5.6). Due to the allowance of the z component, the in-plane wave vector $\mathbf{k}+\mathbf{h}$ is free from the constraint of the energy conservation and can take a large value, independent of ω. Even for a very small change $\Delta\boldsymbol{\rho}$ of the observation point, $\Delta\boldsymbol{\rho}\cdot\mathbf{h}$ can then be large and introduces an appreciable phase change in the exponential and hence an observable intensity contrast.

VI. CONCLUDING REMARKS

It would be worthwhile to compare the local field excited near the periodic array of spheres with that near a single sphere in free space. The maximum intensity of the local field of an isolated sphere is oscillatory as a function of ω. A peak occurs at the frequency of the Mie resonance due to the excitation of a photonic virtual bound state. For the sphere of $\varepsilon=1.6^2$, the Mie resonance in the lower frequency region is found to be at $\omega=0.50$, 0.70, 0.92, 1.11, and so on. With discrepancies of only a few percent, these are just the frequencies at which the scattering phase shifts of M spherical waves present an abrupt and substantial jump of the order of π. It is interesting to note that, in the lower frequency region of $\omega<1.5$ considered in this paper, the Mie resonance of the N waves fails to manifest itself in the maximum-intensity plot, for the damping constant of N virtual-bound states is roughly twice as large as that of the M. Also the half-widths of the peaks of M resonance are generally of the order of $\omega\simeq0.1$, i.e., more than 10 times as large as those of the 2D photonic bands, estimated from the peak width of Fig. 10. Because of this, the lowest two peaks of the maximum intensity are hardly recognizable as distinct peaks. The magnitudes of the resonant local field are suppressed accordingly. For example, for the resonances mentioned above, we find

$|\mathbf{E}|^2_{max} \cong 3.0$, 7.0, 10.5, and 17.5, respectively, on the top of the sphere on the forward-scattering side. These values are much less than those shown in Fig. 3. Thus, the profile and magnitudes of the enhanced near-field images of the present paper may not simply be explained by the single-sphere scattering. We have indeed demonstrated that the closed channels of the NN shell, which carry the information of the array, explain successfully the main features of the enhancement of the low-frequency resonances. Thus, the origin of the near-field image treated in this paper is none other than a sort of morphology-dependent resonance of a periodic array of spheres in contact.

In this paper we have examined the local field in the exterior region of the arrayed spheres. Symmetry consideration upon the photonic band has been shown to be very fruitful. The symmetry-adapted basis functions, as combined with some of the numerical data, could reproduce all the essential features of the resonant near-field images. Based upon the fundamental understanding of this paper, it would be intriguing to study the local field in the interior region. This may be an important topic when the confinement effects of photonic crystals are to be made use of in the nonlinear optics. One might also wonder if a substrate holding latex particles influences the resonant behavior. These problems are currently under study and will be reported in the near future.

Finally, a comment is in order for the comparison with experiments using SNOM. Quantitatively reliable comparison would require some of the sophistication of the present theory by taking into account the actual shape of the SNOM tip and its perturbation on the probing electric field. Although the refinement along this line was not tried, the time reversal symmetry looks to hold in this case too and the calculation of the local field may still be a useful way of approaching the actual near-field profiles. We hope to report the comparison of the present theory with experiments in a future work.

*Electronic address: hmiyazak@olive.apph.tohoku.ac.jp

[1] For fundamental ideas and properties of photonic lattices, see J. D. Joannopoulos, R. D. Meade, and J. N. Winn, *Photonic Crystals* (Princeton University Press, Princeton, 1995); *Photonic Band Gaps and Localization,* edited by C. M. Soukoulis (Plenum, New York, 1993); *Photonic Band Gap Materials,* edited by C. M. Soukoulis (Kluwer, Dordrecht, 1996); P. M. Hui and Neil F. Johnson, in *Solid State Physics,* Vol. 49, edited by H. Ehrenreich and F. Spaepen (Academic, New York, 1995), p. 151.

[2] K. Ohtaka, Phys. Rev. B **19**, 5057 (1979).

[3] W. Lamb, D. Wood, and N. W. Ashcroft, Phys. Rev. B **21**, 2248 (1980).

[4] K. Ohtaka, J. Phys. C **13**, 667 (1980).

[5] E. Yablonovitch, J. Opt. Soc. Am. B **10**, 283 (1993).

[6] A. Mekis, J. C. Chen, I. Kurland, S. Fan, P. R. Villeneuve, and J. D. Joannopoulos, Phys. Rev. Lett. **77**, 3787 (1996).

[7] E. Özbay, A. Abeyta, G. Tuttle, M. Tringides, R. Biswas, C. T. Chan, C. M. Soukoulis, and K. M. Ho, Phys. Rev. B **50**, 1945 (1994).

[8] E. Özbay, E. Michel, G. Tuttle, R. Biswas, K. M. Ho, J. Bostak, and D. M. Bloom, Opt. Lett. **19**, 1155 (1994).

[9] H. S. Sözüer, J. W. Haus, and R. Inguva, Phys. Rev. B **45**, 13 962 (1992).

[10] K. Ohtaka, T. Ueta, and K. Amemiya, Phys. Rev. B **57**, 2550 (1998).

[11] K. Ohtaka and Y. Tanabe, J. Phys. Soc. Jpn. **65**, 2265 (1996).

[12] K. Ohtaka and Y. Tanabe, J. Phys. Soc. Jpn. **65**, 2670 (1996).

[13] K. Ohtaka and Y. Tanabe, J. Phys. Soc. Jpn. **65**, 2276 (1996).

[14] K. Ohtaka, T. Ueta, and Y. Tanabe, J. Phys. Soc. Jpn. **65**, 3068 (1996).

[15] D. Courjon and C. Banier, Rep. Prog. Phys. **57**, 989 (1994).

[16] C. Girard and A. Dereux, Rep. Prog. Phys. **59**, 657 (1996).

[17] D. Van Labeke and D. Barchiesi, J. Opt. Soc. Am. A **9**, 732 (1992); Opt. Commun. **114**, 470 (1995).

[18] D. Barchiesi and D. Van Labeke, J. Mod. Opt. **40**, 1239 (1993).

[19] A. Madrazo and M. Nieto-Vesperinas, J. Opt. Soc. Am. A **14**, 618 (1997).

[20] S. M. Norton, T. Erdogan, and G. M. Morris, J. Opt. Soc. Am. A **14**, 629 (1997).

[21] C. Girard, X. Bouju, and A. Dereux, *Near-Field Optics,* Vol. 242 of *NATO Advanced Study Institute Series E: Applied Sciences*, edited by D. Pohl and D. Courjon (Dordrecht, Kluwer, 1993), p. 199.

[22] K. Ohtaka, H. Miyazaki, and T. Ueta, J. Mater. Sci. Eng. B **48**, 153 (1997).

[23] J. A. Stratton, *Electromagnetic Theory* (McGraw-Hill, New York, 1941), p. 397.

[24] M. Inoue, K. Ohtaka, and S. Yanagawa, Phys. Rev. B **25**, 689 (1982).

[25] For the group theory used in solid-state physics, see, e.g., T. Inui, Y. Tanabe, and Y. Onodera, *Group Theory and Its Applications in Physics* (Springer, Berlin, 1990), p. 1; see its Appendixes, for the character tables of the groups C_{6v} and C_{1h}. For the group theory of photonic bands, see, e.g., Ref. 13.

[26] N. Stefanou, V. Karathanos, and A. Modinos, J. Phys.: Condens. Matter **4**, 7389 (1992).

[27] W. M. Robertson, G. Arjavalingam, R. D. Mead, K. D. Brommer, A. M. Rappe, and J. D. Joannapoulos, Phys. Rev. Lett. **68**, 2023 (1992); J. Opt. Soc. Am. B **10**, 322 (1993).

[28] The precise coefficients that are estimated from Fig. 6 are $C^\sigma = -0.96e^{0.23\pi i}$, $C^\pi = -0.28e^{0.35\pi i}$, and $C^z = 1.36e^{-0.26\pi i}$ for the resonance at $\omega = 0.71$ and $C^\sigma = 0.54e^{0.15\pi i}$, $C^\pi = -1.7e^{-0.01\pi i}$, and $C^z = -1.11e^{-0.35\pi i}$ for the resonance at $\omega = 0.85$. The 2NN contribution for $\omega = 0.85$ is $C^\sigma = 0.09e^{0.10\pi i}$, $C^\pi = -0.22e^{-0.07\pi i}$, and $C^z = -0.11e^{-0.40\pi i}$. Using these values, as combined with Tables I and II, Figs. 4(a) and 4(b) are reproduced perfectly.

[29] Equation (5.6) can be reproduced from the general expression of the transmission and reflection coefficients given in Sec. II. The necessary step for that is to retain only the subspace of $l=1$ in the spherical-wave formulation and to take the limit $\omega a \ll 1$.

[30] If we assume $\varepsilon = 1.6^2$ even in the long wavelength limit, we find $\alpha = 0.34 a^3$ from Eq. (5.1). The maximum value of $|(\mathbf{E}_s)_y(\mathbf{r})|$ attained at $\boldsymbol{\rho} = (0,0)$ is then calculated to be 0.18 for the incident light of unit amplitude. It is the mainly cross term $\mathbf{E_0(r)}^* \cdot \mathbf{E}_s(\mathbf{r})$ that produces the contrast in $|\mathbf{E_0(r)} + \mathbf{E}_s(\mathbf{r})|^2$, i.e., $|\mathbf{E_s(r)}|^2$ is negligible.